Contents lists available at ScienceDirect

SLAS Technology

Biomimetic scaffolds using triply periodic minimal surface-based porous structures for biomedical applications

Raffaele Pugliese [a],[*], Serena Graziosi [b]

[a] *NeMO Lab, ASST GOM Niguarda Cà Granda Hospital, Milan, Italy*
[b] *Department of Mechanical Engineering, Politecnico di Milano, Milan, Italy*

ARTICLE INFO

ABSTRACT

The design of biomimetic porous scaffolds has been gaining attention in the biomedical sector lately. Shells, marine sponges, shark teeth, cancellous bone, sea urchin spine, and the armadillo armor structure are examples of biological systems that have already been studied to drive the design of innovative, porous, and multifunctional structures. Among these, triply periodic minimal surfaces (TPMSs) have attracted the attention of scientists for the fabrication of biomimetic porous scaffolds. The interest stems from their outstanding properties, which include mathematical controllable geometry features, highly interconnected porous architectures, high surface area to volume ratio, less stress concentration, tunable mechanical properties, and increased permeability. All these distinguishing features enable better cell adhesion, optimal integration to the surrounding tissue avoiding stress shieldings, a good permeability of fluid media and oxygen, and the possibility of vascularization. However, the sophisticated geometry of these TPMS-based structures has proven challenging to fabricate by conventional methods. The emergence of additive manufacturing (AM) and the enhanced manufacturing freedoms and flexibility it guarantees could solve some of the bottlenecks, thus leading to a surge of interest in designing and fabricating such structures in this field. Also, the feasibility of using AM technologies allows for obtaining size programmable TPMS printable in various materials, from polymers to metal alloys. Here, a comprehensive overview of 3D-printed TPMS porous structures is provided from a design for additive manufacturing (DfAM) and application perspective. First, design strategies, geometry design algorithms, and related topological optimization are introduced according to diverse requirements. Based on that, the performance control of TPMS and the pros and cons of the different AM processes for fabricating TPMS scaffolds are summarized. Lastly, practical applications of 3D-printed biomimetic TPMS porous structures for the biomedical field are presented to clarify the advantages and potential of such structures.

1. Introduction

In nature, there are a plethora of porous architectures with outstanding performances and multi-functionalities, such as bone, corals, honeycombs, woods, shells, and sponges, among others [1]. Such natural systems have inspired and motivated mathematicians, materials scientists, and engineers to design and develop bioinspired porous architecture materials for revolutionary applications ranging from civil engineering to biomedicine [2–6] (Figs. 1A-E).

Materials with programmable features are commonly known as "metamaterials" [13]. Among these, of particular interest are triply periodic minimal surfaces (TPMSs), which attracted the attention of scientists for the fabrication of biomimetic porous scaffolds due to their mathematically controlled fascinating geometries, highly interconnected porous architectures, and tunable mechanical features [14].

TPMSs and their evolutions have been amply studied in the literature because they are present in many biological systems [15]. They are surfaces that locally minimize surface area for a given boundary such that the mean curvature at each point on the surface is zero [16]. These surfaces have additional distinctive geometrical features. They are smooth surfaces without sharp edges or corners, and they can be used to split the space into 3D periodic, non-intersecting, and, as already underlined, highly-interconnected domains [14]. There are various methods to identify the nodal coordinates that make up a minimal surface [17–20]. One such method is the Enneper-Weierstrass representation, which calculates the nodal coordinates of a TPMS by analyzing the integrals of its Weierstrass function [20]. Another approach is reported by Brakke [17], who created the computer program Surface Evolver, which uses the finite element method to generate minimal surfaces numerically. The Surface Evolver considers the minimum achievable area bounded by one of

---

Fig. 1. A) Photograph of the butterfly Callophyrus rubi and SEM image of the gyroid microstructure found within its wings. Reproduced with permission from Ref. [7]. CC BY NC 4.0. B) Sea urchin and SEM image of its Schwarz nanostructure. Reproduced with permission from Ref. [8]. CC BY 4.0. C). The unique free-from envelope of Kunsthaus Graz, Austria. Reproduced with permission from Ref. [9]. CC BY 4.0. D). The bending façade of the One Ocean Thematic Pavilion in Yeosu, South Korea. Reproduced with permission from Ref. [9]. CC BY 4.0. E) Medical bandage inspired by spider silk fibroin. Image from Shutterstock by Adji Koesoemowidodo. F) Photographs of Hermann Schwarz and his student G) Edvard Rudolf Neovius. Reproduced with permission from Ref. [10]. CC BY 4.0. H) The Alan Hugh Schoen lattice fundamental domain, [11]. CC BY 4.0. Models of triply periodic minimal surfaces of I) diamond, L) gyroid, and M) Schwarz-P. Reproduced with permission from Ref. [11]. CC BY 4.0. N) The monumental NASA technical note of Alan Hugh Schoen, where the preliminary study of partitioning three-dimensional Euclidean space into two interpenetrating labyrinths by intersection-free infinite periodic minimal surfaces (IPMS) is provided. Reproduced with permission from Ref. [12]. CC BY 4.0.

Coxeter's kaleidoscopic cells as the fundamental unit [21], which is then repeated through symmetry operations to form a TPMS. However, the simplest and most used method to produce minimal surfaces-like topologies is using level-set approximation equations expressed as Fourier series [18].

Compared to others, TPMS-based structures have three significant merits: (1) the whole structure can be precisely expressed by mathematical expression; (2) adjusting the function parameters can directly control primary performances, such as porosity or volume-specific surface areas; (3) their structures are highly interconnected with pores, which repre-

sents a significant advantage for specific applications. Based on these merits, more and more research attention has been paid to TPMSs.

The first mention of TPMSs in literature dates back to 1865 when the German mathematician Hermann Schwarz introduced his monumental treatise on the primitive and diamond surfaces [22], followed by a surface described by his student Edvard Rudolf Neovius in 1883 (Figs. 1F-G). Exactly 100 years later, Alan Hugh Schoen reported several other TPMS-based surfaces [12] (Figs. 1H-M). As reported by Schoen himself [11]: *"Because I was beginning to receive not-so-subtle pressure from NASA headquarters to do something 'useful', I decided to apply my analysis of these tilings to the design of expandable spaceframes, including one based on the Laves graph (later on named gyroid)"* (Fig. 1N). This latter is one of the most interesting TPMS, which is still being investigated intensively for its topology-driven properties in different fields. For readers interested in a more comprehensive overview of the discovery and design of TPMSs, we recommend consulting the following articles [10,23–27].

Thanks to these curious minds and their serendipitous discoveries, the field of TPMS expanded at an accelerating pace. In recent decades to fulfill the demands of diverse applications and to mimic natural porous structures, homogeneous TPMSs, graded TPMSs, heterogeneous TPMSs, and multiscale TPMSs were designed [14]. This is particularly relevant for biomedical, tissue engineering, and regenerative medicine applications, where we deal with complex and multi-functional structures such as tissues and organs. In this context, TPMSs allow (1) an optimal integration to the surrounding tissue avoiding stress shieldings when implanted [28], (2) better cell adhesion, proliferation, and growth for repairing damaged tissues [29], (3) a good permeability of metabolic supply, fluid media and oxygen, and (4) vascularization of newly formed tissue [30]. In addition, due to their tunable mechanical properties, biomimetic porous structures can be designed to match the mechanical properties of native tissue and organs, thus avoiding their rejection as "non-self human structures". Besides, optimized TPMS-based structures have been included in the so-called "shellular" class as more valid alternatives than hollow truss structures in developing ultralow density materials [31].

However, the sophisticated geometry of these TPMS-based structures has proven challenging to fabricate by conventional methods. Thanks to the progressive advancement in manufacturing techniques, such as additive manufacturing (AM), and the enhanced freedoms and flexibility it provides, some manufacturing constraints were overcome, thus leading to a surge of interest in designing and fabricating complex structures [14,15,32,33]. Also, the feasibility of using AM technologies allowed for obtaining size-programmable TPMS printable in various materials, from polymers to metal alloys, paving the way for the emergence of the "materials-by-design" field [34–37].

Thus, AM has pushed the development and fabrication of topologically complex structures at different length scales, from the nanoscale to the macroscale. As reported by Al-Ketan et al., [37] these advancements facilitated the emergence of a new design for additive manufacturing (DfAM) paradigm in which complex morphological lattices are integrated within functional components to reduce weight, enhance mechanical and physical properties, enable multi-functionality, and facilitate personalization.

However, there are still many open challenges to be addressed in the DfAM of TPMS-based scaffolds: (1) how to guide the tuning of lattice design variables, such as cell type, unit cell size, and volume fraction in relation to the selected material and design needs; (2) how to support the selection of the proper lattice topology, for instance, according to the anatomic region of interest; (3) how to overcome current manufacturing limits related to the printing of soft materials, which are of particular interest for regenerative therapies of soft-like tissues as brain and spinal cord, or tissues that undergo large elastic deformations (i.e., heart, skin, peripheral nerve tissue, and muscle).

In light of this, a comprehensive overview of 3D-printed TPMS porous structures is provided here. Section 2 addresses the main DfAM aspects related to generating and optimizing TPMS-based topologies.

Based on that, in Section 3, we overview their performance, while the pros and cons of the different manufacturing processes employed to fabricate them are analyzed in Section 4. Lastly, applications of 3D-printed biomimetic TPMS-based porous structures for the biomedical field are discussed in Section 5 to clarify the advantages and highlight their potential. In Section 6, conclusions are drawn.

2. A DfAM perspective on TPMS

2.1. Mathematical modelling of TPMS-based structures

A surface is triply periodic when translational symmetries characterize it along the three principal directions [4,15,16]. This type of surface can be exploited to graphically model the periodic (cubic) morphology of block copolymers [38]. Also, upon certain thermodynamic conditions, these blocks create periodic interfaces (i.e., the so-called intermaterial dividing surface [39]) with a constant mean curvature [38]. Hence, the need to study the behaviour of such materials at the microscale has significantly pushed the search for the proper strategy to model these constant-mean-curvature periodic surfaces, able to regularly split the space into interconnected domains, each representing a specific copolymer block [39].

These triply periodic constant-mean-curvature surfaces can be seen as deformations of TPMSs [31]. The "minimal surface" class solves what is known in computational differential geometry as the Plateau problem, i.e., extending a curve (the boundary) through a surface whose topology is the one having, compared to all those surfaces generated through a local perturbation of the "system", the minimal area [37,38,40]. However, their area is not an absolute minimum but a local one [41]. Indeed, the leading property that must be preserved for this type of surface is that they have a mean curvature equal to zero at any point [15,38]. It is also worth mentioning that for a boundary curve, there could be multiple minimal surfaces [40].

The most studied TPMSs are those without self-intersection, discovered in the eighties [41]. They are indeed the most relevant from a mathematical and natural science point of view. The TPMSs analysed today are thus universally recognised as not self-intersecting, i.e., they separate a volume into two or more labyrinthine domains [38]. Although several methods have been studied to represent TPMSs [38], as already discussed in Section 1, level-set surfaces have been proposed as a valid approximation to model, for example, the previously mentioned interfacial surfaces of block-copolymers [38,42] starting from a minimal surface. They are generally non-self-intersecting and smooth, except for specific conditions [38].

Level surfaces of triply periodic functions with cubic symmetry can be expressed through the following implicit equation [38]:

$$F(x, y, z) = t \qquad (1)$$

where t is a constant determining the offset of the level surface (or isosurface) from the $t = 0$ condition, which is the base surface[38]. $F(x, y, z)$ is the function which identifies a specific family of level surfaces. It is expressed in trigonometric terms to preserve the cubic symmetry with respect to the x, y, and z axes of the Cartesian frame[43].

Studies have demonstrated that using Fourier terms to express this function is a simple but analytically valid approach [39]. The advantages of using level-set surfaces are two-fold [37]: (1) they support the modelling of triply periodic topologies, and (2) they allow the control of how these surfaces should change to accommodate different volume fraction values. Also, being these functions expressed using the Cartesian system, they can be easily modified [43].

For example, a well-known level set family of equations is the following [43]:

$$F_G(x, y, z) = sin\left(2\pi n_x \frac{x}{L_x}\right) \cdot cos\left(2\pi n_y \frac{y}{L_y}\right) + sin\left(2\pi n_y \frac{y}{L_y}\right)$$
$$\cdot cos\left(2\pi n_z \frac{z}{L_z}\right) + sin\left(2\pi n_z \frac{z}{L_z}\right) \cdot cos\left(2\pi n_x \frac{x}{L_x}\right) = t \qquad (2)$$

In this formula, n_i and L_i (for $i = x, y, z$) represent the number of cell repetitions and the linear dimension of the design space, respectively, for each principal direction. The condition $t = 0$ and n_i=1 represents an approximation to the Schoen's gyroid (G) minimal surface (Fig. 1) where L_i can thus be used to determine the dimensions of the unit cell. By modifying the t value in Eq. 2, a family of surfaces can be created, starting from the Schoen's gyroid (G) minimal surface. To create solid domains starting from level-set equations, such as Eq. 2, two main approaches are here discussed, called in the field of architected materials, "network" or "solid" (namely also as "skeleton") the first, and "matrix" or "sheet" the second [38,44]. To explain how these two approaches work, we will initially consider, as an example, a cubic unit cell of 1mm in length (i.e., n_i=1, $L_i = 1mm$, Eq. 2). Then we will move to arrays of unit cells, analyzing the outputs and the information provided by software tools such as, MSLattice [44] and Flat Pack [43], which, as discussed later, can be used to support the design of these structures.
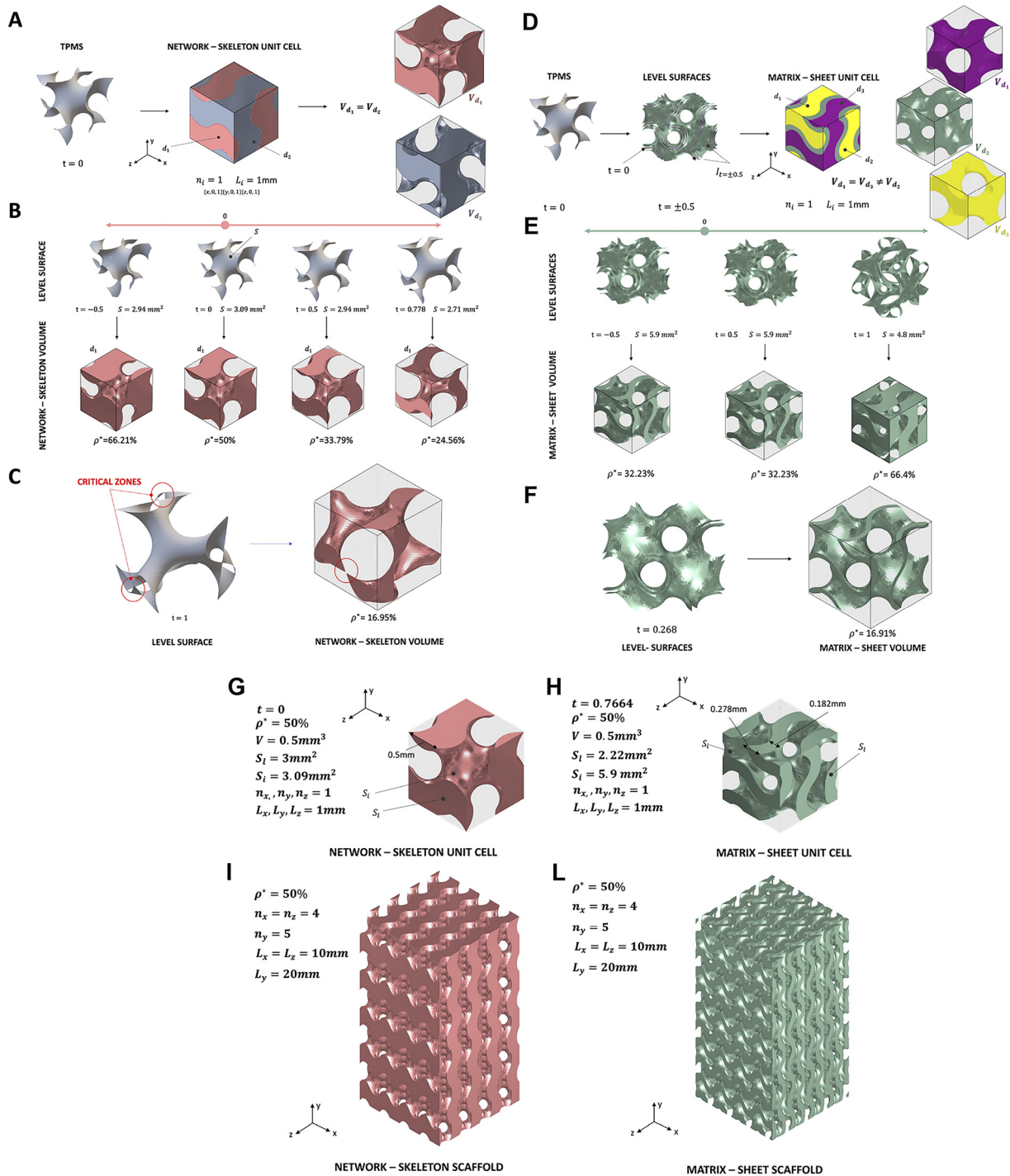
The "network" or "solid" approach uses the level-set surface to split the domain into two main subdomains. When $t = 0$, which is the condition approximating the minimal surface, the space is divided into two continuous regions [38]. This cubic volume is thus split by the gyroid surface into two equal subdomains, leading to a relative density (ρ^*) equal to 50% (Fig. 2A) if we consider one sub-domain as solid and the other as void. The relative density can indeed be expressed as a volume fraction, i.e., as the ratio between the volume of the solid subdomain and the volume of the overall design space (e.g., the cubic domain in Fig. 2A). The condition $\rho^* = 50\%$ for $t = 0$ is valid not only for the Schoen's gyroid (G) TPMS but, as demonstrated by Lambert et al., [38] also for the Schwarz's primitive (P) and the diamond (D). The TPMS having the property of splitting the space into congruent and interchangeable regions are defined as balanced surfaces [18,37] to distinguish them from those classified as unbalanced (the Schoen I-WP) that split the space into not congruent solids [44]. Hence, in the case of the "network" or "solid" approach, as solid domains, we can select the one described by one of these two conditions:

$$F(x, y, z) > t \ or \ F(x, y, z) < t. \qquad (3)$$

By modifying the t value (t is not a distance), either positively or negatively, the volume of these subdomains will vary. Hence, the ρ^* will change, as shown in Fig. 2B. The newly generated surface now has a mean curvature that is not zero. When the t value is increased too much (i.e., low ρ^* values are required), for network-solid surfaces, there are "threshold" limits over which the surfaces and, thus, the solid start to become disconnected (Fig. 2C). The connectivity problem at a low relative density of "network-solid" TPMS is a well-known issue in the literature (e.g., see Refs. [38,45–47]) that can be solved by modifying the original $F(x, y, z)$ function accordingly as in Ref [46,47] or, as we will see later, by applying the "matrix" or "sheet" approach.

The superficial area values provided in Fig. 2B (obtained for a cubic volume of 1 *mm* length) demonstrate that the biggest area is the minimal surface. This surface is important because it is the one that could be relevant for issues related to, e.g., the permeability of a scaffold (see Section 3.2 for further details).

Hence, to create a solid volume, in the case of the "network-solid" approach, once the dimensions of the design space are defined, the selected level-set surface determines how this design space will be split. Instead, in the case of the "matrix" or "sheet" approach, the solid domain is the one limited by two level-set surfaces evaluated at $\pm$ t, i.e., -t≤$F(x, y, z)$ ≤ t [44]. This is the most common case in literature, as discussed in Ref [37], where the lattice is generated starting from a hypothetical surface evaluated at t=0, and then "t" is symmetrically changed with respect to this "0" condition to obtain solids having different volume fractions. However, further configurations can be obtained by evaluating these "limiting" surfaces at different t values (e.g., $-1.7 \leq F(x, y, z) \leq -2.3$, as shown in Ref [37]). Another approach for creating solid domains, which recall the "matrix" or "sheet" strategy but which leads to different outputs, concerns the thickening of the base

Fig. 2. The network-solid approach for generating the level surfaces and related solid volumes. A) The two equal volumes generated by the gyroid TPMS. B) How the level surface and the d1 solid volume change by modifying the t value (the d2 volume will change inversely). The value t=0.778 has been selected for comparison with Ref [38]. *S* represents the surface area. C) Examples of discontinuities that can appear when a threshold value for t is overcome when designing very low-density structures. D) The three volumes generated by the two surfaces obtained setting $t = 0.5$, i.e., $-0.5 \leq F(x, y, z) \leq 0.5$. E) How the level surface and the solid volume change by modifying the *t* value (it is evident that for $t = \pm 0.5$, the same couple of surfaces is generated). F) The same density value obtained with the "network" or "solid" strategy (Fig. 2C) is obtained here to demonstrate that, in this case, the volume is still continuous. G-H) Comparison between the network-solid and the matrix-sheet unit cell and scaffolds (I-L) at equal ρ^*, n_i, L_i values.

surface by uniformly offsetting it [38], i.e., the surface is thickened by applying a mid-plane offset based on the desired thickness value. The base surface could be the one at t=0 or not. As discussed in Ref [48], especially at large relative densities, the difference between a sheet-based geometry and the one obtained through this thickening procedure of the mid surface becomes significant.

In the "matrix" or "sheet" approach, when $t = 0$, no solid domains are generated. As shown in Fig. 2D, when $t = 0.5$, three sub-domains are obtained starting from a cubic domain ($x = y = z$), two of which are congruent (i.e., $V_{d1} = V_{d3}$). The fact that the two domains have the same volume is a condition that will also be preserved for other t values if these values are considered symmetrically than the $t = 0$ condition. The

closer it is t to the $t = 0$ condition, the bigger the superficial area, and the smaller it is ρ^* (Fig. 2E). For the "matrix-sheet"-based TPMS when used for creating very low-density structure, as explained in Ref [37], the minimum threshold value for t is only related to the manufacturability of the structure in terms of minimum thicknesses allowed. Indeed, at the same relative density of the "network-solid"-based cell (Fig. 2F), in this case, the solid is not-disconnected (Fig. 2F).

Figs. 2G-H show how, for the same $\rho^* = 50\%$, the two approaches lead to volumes having a different topology. The area of the internal and lateral surfaces (S_l and S_i) is also provided. This figure further demonstrates that the t value does not represent the thickness of the solid volumes in both approaches and that the thickness of the generated volumes is not constant.

Moving to a general formalization of Eq. (2), which considers both modalities for creating the solid domains, the following expression can be used, as discussed by Maskery et al., [43]:

$$
F_G(x, y, z) = \left(\sin\left(2\pi n_x \frac{x}{L_x}\right) \cdot \cos\left(2\pi n_y \frac{y}{L_y}\right) + \sin\left(2\pi n_y \frac{y}{L_y}\right) \right.
$$
$$
\left. \cdot \cos\left(2\pi n_z \frac{z}{L_z}\right) + \sin\left(2\pi n_z \frac{z}{L_z}\right) \cdot \cos\left(2\pi n_x \frac{x}{L_x}\right) \right)^m - t^m
$$

$$(4)$$

When $m = 1$, this equation generates a scaffold based on the "network" or "solid" approach, while when $m = 2$, a "matrix" or "sheet" based scaffold is generated. Reference [43] provides all the main implicit equations of the available TPMS (e.g., Primitive, Diamond, Neovius). The term scaffold is used here because n_i and L_i (for $i = x, y, z$) represent, as already underlined, the number of cell repetitions and the linear dimensions of the design space, which in this case is a scaffold, respectively, for each principal direction (Figs. 2I-L).

Nowadays, multiple software tools allow the generation of TPMS scaffolds/lattices, both commercial (e.g., nTopology [49], Gen3D [50]) and free. Examples of free tools are: FLattPack [43], ASLI [51], TPMS Designer [52], Minisurf [53], MSLattice [44] and Region TPMS [54]. Although some of them allow working directly with implicit functions, scaffolds are generated once n_i, L_i, ρ^*, the type of TPMS and the generation strategy (i.e., "network-solid" or "matrix-sheet") are provided as inputs. Through these software tools, scaffolds with a non-uniform ρ^* value distribution can be modelled, as well as multi-morphology TPMS-based scaffolds. Multi-morphology (or hybrid) scaffolds are obtained by properly "combining" level-set surfaces having different topologies, as discussed by Al-Ketan et al., [44] Yang et al., [55] and Novak et al, [48]. Fig. 3A shows some examples of hybrid scaffolds. An overview of modelling and design tools to support the generation of functionally graded lattices (including TPMS-based structures) is provided in Ref. [37,56]. Finally, different design spaces can be selected (not only cubic), and the TPMS-based scaffold can be adapted to conform to complex design domains, for example, when they are used as infill of bones or implants.

Beyond the multi-morphology and graded scaffolds, the porosity and volume-specific surface areas of TPMSs can be further improved by multiscale porous structures [14]. These structures are categorized based on their pore diameter: (1) microporous structures with a diameter less than 2 nm, (2) mesoporous structures with a diameter between 2-50 nm, and (3) macroporous structures with a diameter over 50 nm. However, designing multiscale TPMSs through CAD design algorithms remains a challenge. Although implicit functions can accurately express TPMS, designing multiscale TPMS with a single function is still difficult. The pore sizes of graded TPMS are different but not crossing scales, as the surface would change dramatically if both microporous and macroporous structures were present in the graded TPMS structure.

Classical CAD algorithms rely on Boolean operations to merge multiscale porous structures, but this approach has several disadvantages. Furthermore, Boolean operations are time-consuming and prone to error, especially as TPMS surfaces are often expressed as mesh models with

numerous discrete facets for improved construction accuracy. The complex porous structures also increase the computational burden, which can consume computer memory or result in multiple errors. Additionally, the calculation results from Boolean operations may be incorrect for multiscale TPMSs, leading to separated or broken parts that cannot be fabricated through AM. Efforts have been made to improve the calculation process, but the limitations of 3D Boolean operations for multiscale TPMSs remain [60].

Jiawei et al., [61] proposed a new strategy to generate multiscale TPMS porous structures. The calculation process for 3D multiscale TPMS structures has been streamlined by converting it into a series of 2D operations, improving calculation efficiency. To extract TPMS with smaller pores, the solid areas of TPMS are meshed, and the extracted layers are alternately designated as solid or pore areas. This reconnects areas separated by pores, resulting in a complete multiscale TPMS structure. Using such four levels of TPMS, three scales of pores can be generated. As reported by the authors, the resulting multiscale TPMS structures can be directly utilized in AM, eliminating the need for the time-consuming slicing process. This streamlining of the calculation process not only saves time but also improves the accuracy and integrity of the final TPMS structure.

Alternatively, Li et al., [62] proposed an efficient merging method for constructing multiscale TPMS structures. This method directly merges TPMS with pores of varying scales and uses the Allen–Cahn equation to create smooth surfaces, reducing sharp boundaries and stress concentration. However, this approach is implemented using network-based TPMS rather than sheet-based TPMS. Overall, the complexity of multiscale structures increases as the number of scales increases. Unlike multi-morphology TPMS, there is currently no effective method to describe multiscale TPMS using implicit functions. The use of 3D Boolean operations is limited to simple structures. Therefore, developing more reliable design strategies for multiscale TPMS structures is needed.

2.2. Controlling and extending TPMS-based topologies

Section 2.1 has briefly clarified the main mathematical aspects at the basis of the modelling of TPMS-based porous structures starting from implicit equations. Theoretically, an infinite type of TPMSs can be generated starting from those equations [63], also properly tuning the design parameters available. As explained by Jones et al., [52] the first step for the detailed design of the TPMS-based structure consists of selecting the implicit equation of interest (i.e., the specific TPMS) and then the targeted ρ^* value, which is a fundamental parameter in determining the structure's mechanical behavior, especially in network-skeleton structures [14]. As already introduced, in the case of matrix-sheet TPMS, additional parameters, such as the thickness, can be considered for controlling the structure topology [64]. Once selected the ρ^*, the dimensioning of the structure can start by choosing the proper cell size, also considering manufacturability constraints (e.g., minimum and maximum thickness values). Further additional design parameters could become relevant when looking for specific applications, such as the design of biomimetic scaffolds for bone tissue engineering. An example is represented by the dimensions of the pores [65], i.e., the largest sphere size fitting inside the structure's void domains [58] (Fig. 3B). These dimensions should be tuned to support the transport of nutrients to favour osteointegration. However, despite the software applications already available to generate TPMS-based structures, a proper design tool is lacking to allow direct control of all the design parameters of interest based on the specific application.

The advantage of creating 3D digital models starting from equations has significantly pushed the research focused on extending the range of topologies available. For example, as anticipated in Section 2.1, there are studies focused on supporting the design of multi-morphology structures, such as the one presented by Yang et al., [66], where two methods are proposed to create a smooth transition between regions characterized by different TPMS-based morphologies. Meyer et al. [59] reported
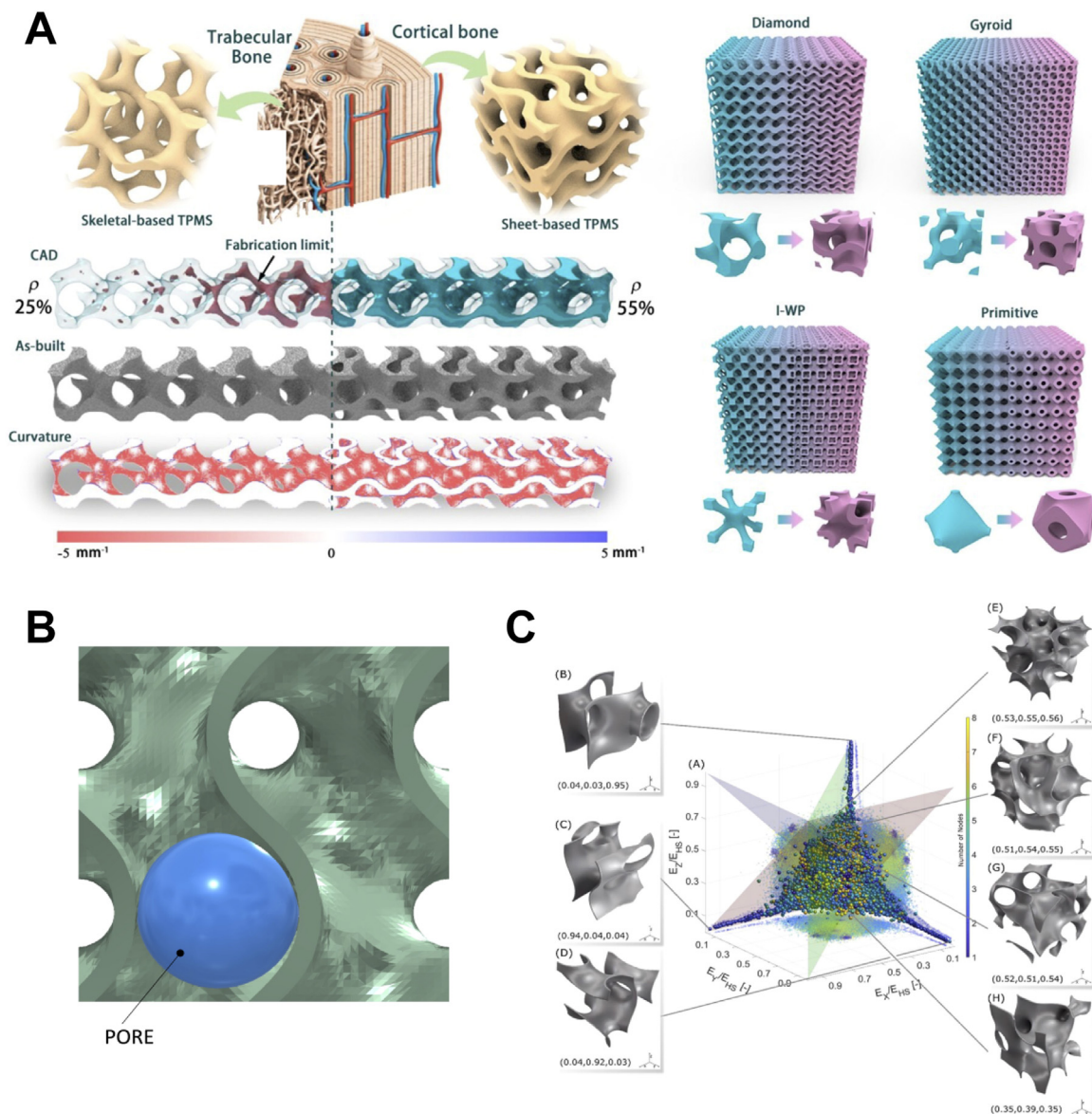
Fig. 3. A) Examples of functionally graded and hybrid TPMS-based structures. On the left a design strategy implemented to mimic the inner structure of bones. On the right, an example of graded structures obtained combining sheet- and skeletal-based (or solid-based) TPMS structures. Reproduced with permission from Ref. [57]. CC BY 4.0. B) Explanation of the design parameter related to the pore size. Image inspired by Ref [58]. C) Example of a structure-property map focused on directional Young's moduli. Reproduced with permission from Ref. [59]. CC BY 4.0.

a systematic approach, based on graph models, to generate new shell-lattice topologies (more than 43,000) (Fig. 3C). Besides, this approach combines machine-learning algorithms to predict the structure-property relationship for targeted macroscopic properties such as elastic and thermal properties.

Concerning computational strategies to optimise TPMS-based structures, studies are still limited [67,68]. Mainly geometric changes to the TPMS topology are applied without a real topological optimization [67]. The point is that, in the case of TPMS-based structures, the topology change occurs by modifying its periodicity [67], as, for example, shown in Ref [39], where multiple morphologies can be obtained starting from a family of level surfaces. Optimization strategies not tailored to manage the complexity of the TPMS morphology would thus require time-consuming computational efforts to preserve its complex microstructure [67]. Besides, it is well-known that conventional topology optimization methods could lead to porous structures that are not easy to manufacture, even with AM [69]. Hence, dedicated optimization approaches

that preserve the TPMS topology peculiarities, solve connectivity issues [70] and are computationally efficient are needed.

In Ref [46], a generative design optimization method is proposed and tested using a gyroid TPMS. As already underlined, in that study, the morphological optimization is performed by introducing a penalty function to avoid those t values, which could lead to discontinuities (see Fig. 2C). In the study [67] the authors have proposed an approach that generates an optimal scale-varying porous structure [67], starting from the intent of minimizing its compliance when used as infill and preserving, as constraints, the distinguishing features of TPMSs (e.g., smoothness, pores, and connectivity). Instead, Strömberg et al., [68] proposed a multi-scale topology optimization strategy based on two density variables, one at a macro level and the other representing the density of the unit cell based on the calculation of the homogenized properties. Finally, Lehder et al., [71] have proposed a graphical multiscale optimization method to drive TPMS-based bone scaffold design. The method starts with defining an objective function, which maximises the pre-

Table 1

Summary of notations using in Gibson and Ashby formulation.

E^*	Relative elastic modulus of the TPMS structure.
E_{latt}	Elastic modulus of the lattice structure.
E_{sol}	Elastic modulus of the material constituting the lattice structure.
ρ^*	Relative density, or volume fraction, of the TPMS structure. ρ^* takes values from 0 to 1, where 1 represents a fully solid structure.
ρ_{latt}	Relative density of the lattice structure.
ρ_{sol}	Relative density of the material constituting the lattice structure.
C_1	Gibson and Ashby pre-factor. It is a geometric parameter and takes values from 0.1 to 4.
n	Values of the power exponent n can range from 1–4. In general, if the stiffness of the cellular material exhibits a quadratic dependence on the relative density such that the exponent n~2, then the material would show a bending-dominated deformation mode.

osteoblast cell growth modelled through level-set equations. This modelling phase considers the isosurface of interest and, as constraints, the pore size (i.e., maximum and minimum allowed pore diameter) and scaffold target stiffness (i.e., a maximum and minimum allowable axial stiffness).

3. Performance of TPMS

The promising mechanical, thermal, optical, energy storage, and crashworthiness performances of TPMS-based porous structures have gained widespread attention in recent years [14,37,42]. As discussed before, the goal of geometry/topology design is not only to generate TPMSs with characteristics similar to those of natural porous architectures but also, based on this, to tune their performance so that they can be successfully applied in different fields.

As this review focuses on TPMS-based porous structures for biomedical applications, important aspects for the control of mechanical and permeability performance useful for designing TPMS scaffolds for tissue engineering are discussed in this section. However, for readers interested in more details on other TPMS performances, we recommend consulting the following articles [72–77].

3.1. Mechanical performance

Among the performance of TPMS that must act as a scaffold to regenerate or replace damaged tissues/organs, mechanical performances are certainly the most important. Regardless of the engineered TPMS porous structure, mechanical performance is required to keep the structures stable and reliable. Furthermore, such structures must have mechanical features that match native tissues. The fundamental mechanical property indexes to pay close attention to are the elastic modulus, compressive modulus, and anisotropic properties. Before choosing a TPMS scaffold configuration, it is essential to remember the following.

As widely investigated by Maskery and colleagues [78], the relative density (ρ^*) is the most crucial influence factor on the elastic modulus for TPMS structures. For TPMS porous structures of the same topology, relative density or volume fraction directly impacts the elastic modulus (Fig. 4A). Hence, adjusting the relative density with the help of the scaling laws can control the elastic modulus. The semi-empirical formulae of Gibson and Ashby [79] describe the relationship between relative density and elastic modulus or plateau stress. Among such formulae, the most important from the perspective of structural design is the relationship between the relative elastic modulus of a cellular structure and its volume fraction:

$$E^* = C_1 \rho^{*n} \tag{5}$$

$$E^* = \frac{E_{latt}}{E_{sol}} \tag{6}$$

$$\rho^* = \frac{\rho_{latt}}{\rho_{sol}} \tag{7}$$

As underlined in Ref [80], for a given loading scenario and in the case of mechanical applications, these equations can be used to drive

the design of lattice structures, such as TPMS-based scaffolds, once the values of the pre-factor and exponent are known (see Table 1 for physical notation of equations). Moreover, they are significant since they indicate a straightforward means by which the modulus of any TPMS structure can be tailored by modifying its relative density or volume fraction. In addition to these formulas, it is worth underling that, starting from the Gibson and Ashby formulation, further properties can also be considered (e.g., see Ref [79]).

The elastic modulus of TPMS lattice structures increases with the number of unit cells, asymptotically approaching an upper bound (Fig. 4B). The incrementally increasing elastic modulus can be attributed to the diminishing effect of cells with free surfaces on the overall stiffness of the TPMS structure, thus giving a more accurate description of the cell deformation as if it were part of a homogeneous porous solid. As reported by Maskery et al., [78,80], the obtained modulus from finite element analysis of a single unit cell results in an underestimation of the stiffness by ~20% (Fig. 4B). Instead, the 4 × 4 × 4 lattice arrangement provides an elastic modulus 0.2% below the upper bound. Hence, this arrangement provides a reasonable estimate of the lattice structure's elastic modulus, with significantly reduced computational expense, thanks to the smaller number of elements required to model, e.g., a 5 × 5 × 5 structure. This aspect is of fundamental importance for investigating and experimental testing such structures and for elucidating relationships between geometry, cell size, and mechanical performance.

Yet, it should be emphasized that the loading orientation applied to the TPMS structure can lead to changes in the elastic modulus (as depicted in Fig. 4A). This means most porous TPMS structures are anisotropic with unequal elastic modulus in different directions. If such structures are used as tissue implants, this parameter should be considered because it could affect their performances (i.e., implanted TPMS may be broken due to anisotropy) [81,82]. However, this aspect has not yet been thoroughly investigated from a clinical perspective, even if engineering studies have become available [83]. Hence, it is also necessary to control the anisotropy properties, the relative density, and the elastic modulus simultaneously, especially if the scaffolds must bear uniform loading in different directions. To this end, Jiawei Feng et al., [64] performed several analyses to design isotropic TPMS structures. The authors assessed the influences of offset wall thickness (0.2-1 mm) *versus* anisotropy in sheet Primitive (P), Gyroid (G), Diamond (D), and I-Wrapped Package (I-WP). As shown in Fig. 4C, the Zener anisotropy indexes (a dimensionless number used to quantify the anisotropy for cubic crystals) of sheet P and I-WP TPMSs decrease with the growth of the wall thickness.

On the contrary, the Zener anisotropy indexes of G and D gradually grow as the wall thickness increases. For the sheet-based gyroid, for wall thickness equals 0.6 mm and 0.8 mm, the Zener anisotropy indexes are 0.9860 and 1.0052, respectively, meaning that gyroid-based porous structures own approximately isotropy properties with similar elastic modulus in different directions. An isotropic diamond structure can be obtained by increasing the wall thickness, and the same occurs for the primitive structure. However, raising too much the wall thickness will make the porous structures almost fully solid, leading to the loss of those peculiarities, which characterize low-density materials. In-
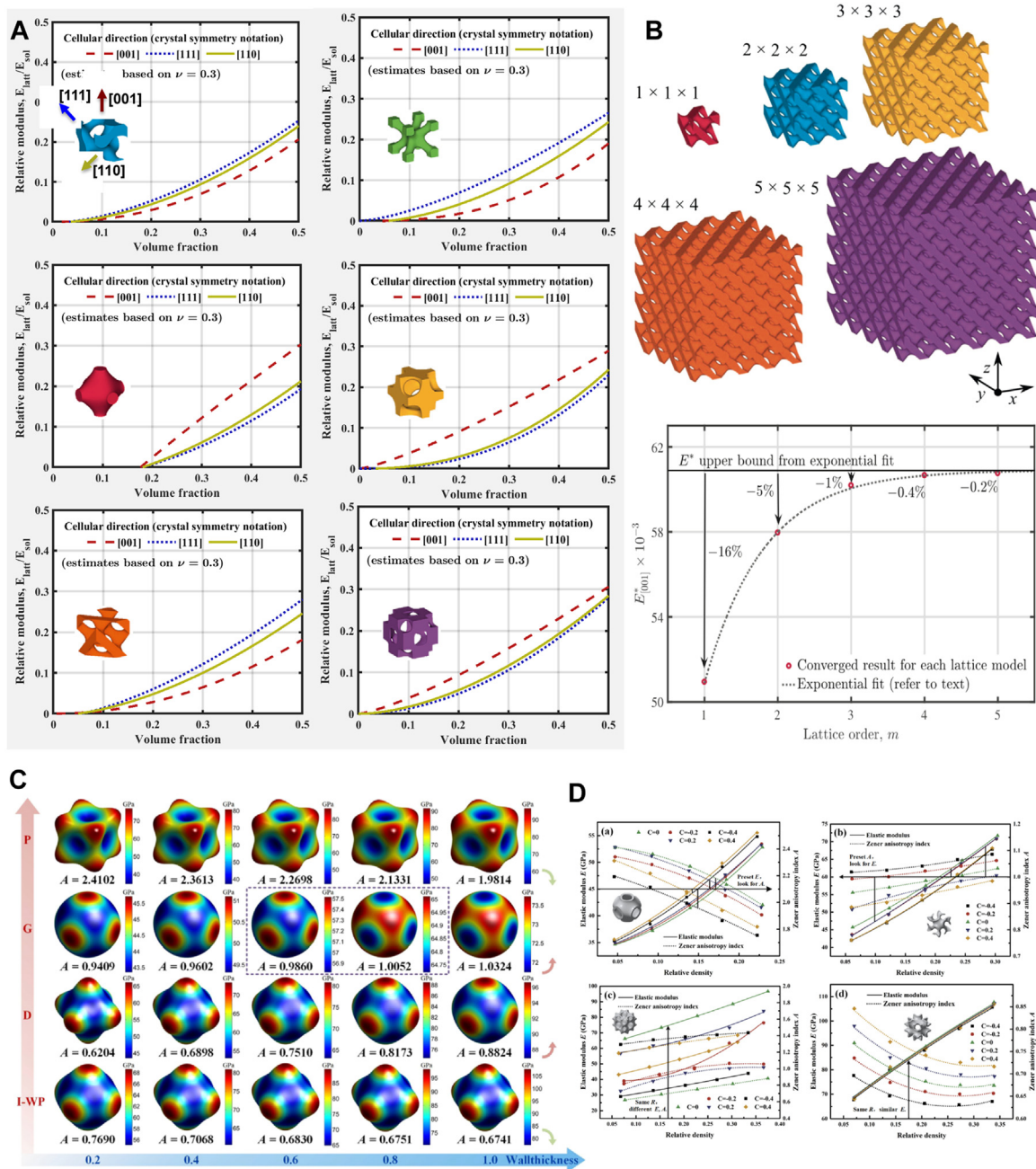
Fig. 4. A). Curves of relative elastic modulus (E^*) as functions of volume fraction for gyroid, primitive, diamond, BCC, Neovius, and OCT along the [001, *z*-direction], [111, *y*-direction], and [011, *x*-direction] loading directions. B) Example of diamond TPMS structures comprising $1 \times 1 \times 1$ to $5 \times 5 \times 5$ unit cells with $\rho^* = 0.3$ and evolution of relative elastic modulus with increasing lattice unit cells. Reproduced with permission from Ref. [78]. CC BY 4.0. C) Anisotropy map of primitive (P), gyroid (G), diamond (D), and I-wrapped package (I-WP) structures with wall thickness ranging from 0.2 to 1 mm. D) The relative density influences on elastic modulus and anisotropy: (a) sheet P, the arrow from left to right means to look for TPMS with the same E but different A; (b) sheet G, the arrow from right to left means to look for TPMS with the same A but different E; (c) sheet D, the arrow from down to up means to look for TPMS with the same relative density but different E and A; (d) sheet I-WP. Reproduced with permission from Ref. [64]. CC BY 4.0.

stead, isotropic sheet I-WP can be obtained with small enough wall thicknesses. However, in the case of small dimensions, manufacturability issues could occur.

To further verify the relative density influences on elastic modulus and anisotropy, the authors reported the influence of the variation of the parameter *C* (i.e., the *t* parameter in Section 2.1) (see Table 1) and offset wall thickness (Fig. 4D). Similarly to the relationship between relative density and elastic modulus, the distribution of Zener anisotropy indexes can also be fitted with smooth curves. For the sheet TPMSs with the same parameter *C*, the relationship between relative density and elastic

modulus can still be expressed by scaling laws. However, for the same type of TPMS with different *C* values, the elastic modulus of the porous structures with the same relative density is not equal.

In addition, the anisotropy of TPMSs with the same relative density is also different. Therefore, as highlighted by the authors, the relative density or scaling laws are not precise enough to control the mechanical properties of TPMS structures. The topology of the same type of TPMS unit is also altered when *C* is changed. Hence, for specific applications with defined elastic modulus requirements, a combination of the parameter *C* and wall thickness must be found, along with a series of ideal

parameters that must be selected based on the anisotropy requirements (if necessary).

Recently, Yang et al., [84] proposed a skew transformation (ST) to distort TPMS lattices at the design stage, modify their mechanical anisotropies and tailor their deformations under uniaxial loading, thus overcoming the cubic symmetry-limiting of the standard TPMS useful for medical applications. As reported before, the anisotropy has been tuned by changing the wall thickness or relative density of a TPMS lattice. Still, these methods might change the lattice's volume fraction and are unsuitable for achieving a target mechanical property with the target volume fraction. Instead, in the ST method, the lattice Young's modulus and anisotropy can be tailored under a constant volume fraction. Such a method can be used to change the anisotropy independently of the volume fraction to match that of native tissue. In addition, using this method, the modulus anisotropies of TPMS can be tuned by a hybrid of two types of substructures with different anisotropies.

Furthermore, Khaleghi et al., [85] investigated the directional elastic modulus of seven TPMS structures (i.e., Schwarz-P, IWP, gyroid, diamond, FKS, FRD, and Neovius). The authors indicated that the stiffness tensor of all these structures is almost cubic symmetric and that the strong and weak directions in IWP, gyroid, FRD, FKS, and diamond are diagonal and axial, respectively. In contrast, Schwarz-P and Neovius structures show a reversed order. To achieve a uniform directional elastic modulus and the lowest state of anisotropy, they designed a hybrid structure consisting of Schwarz-P/Neovius and each of the other five structures in laminated or matrix-spherical inclusion form finding an optimal combination ratio of the parent structures that can lead to the lowest state of anisotropy of the elastic modulus in a hybrid structure.

Overall, the relative density is widely adopted as the main design parameter to directly control the elastic modulus of TPMS structures. However, considering the increasingly complex requirements of real applications of such structures, such as tissue implants or bone grafts that bear loads in different directions, it is necessary to design both the elastic modulus and the anisotropy. For TPMS-based cells whose behavior is isotropic (i.e., gyroid and diamond), the performance can be controlled by tuning the wall thickness. Instead, for those TPMS-based cells whose mechanical behavior is far from being isotropic (such as the primitive and I-WP), it will be necessary to find appropriate ratios (between C and the wall thickness values) to generate TPMSs with an adequate elastic modulus, bearing in mind that the final scaffold topology can be still considered as a porous structure. In addition, to overcome the cubic symmetry-limiting of the standard TPMS, the ST method or the hybridization of two TPMS types can be exploited to change the anisotropy independently of the volume fraction.

Finally, the importance of the different compressive behavior and failure mechanism of skeletal-TPMS, strut-TPMS, and sheet-TPMS should not be underestimated before choosing a suitable TPMS scaffold configuration for specific application needs.

For instance, Guo et al., [86] reported a comparison between Skeletal-TPMS and strut-TPMS lattices of four kinds of TPMS, namely Gyroid (G), Schwarz Diamond (D), Schwarz Primitive (P), and IWP. The simulation and experimental results showed that when the relative density is below 0.5, the P- structure exhibits the highest Young's modulus and yield strength compared to other structures, meaning it is the stiffest and strongest. On the other hand, the IWP structure has the lowest stiffness and strength despite having the largest connectivity among the other structures, indicating that a larger number of nodes does not equate to increased rigidity. Furthermore, the authors used the power law index (n) to assess the deformation behavior of porous materials [87], but the simulation and experiment results suggest that the P-structure is less affected by relative density, as the power law index n in the Young's modulus of skeletal-P and strut-P is 1.437 and 1.120, respectively, while it is over 2 for other structures. Similarly, the power law index n in the yield strength for skeletal-P and strut-P is 1.250 and 1.100, respectively, while it is bigger than 1.6 for the other structures, making the Schwarz Primitive structure much stronger than others. This

is because such a structure has a stretching-dominant mode of deformation, while the other three structures have a bending-dominant one. In addition, using finite element analysis, the authors showed that Skeletal-TPMS and strut-TPMS have different deformation mechanisms under compression. The skeletal-G exhibited a continuous form of stress concentration in the form of a spiral strip, while strut-G had a discrete point at the ligament junction. The stress concentration of skeletal-D was in the form of a ring in the middle part of the ligament, while strut-D had a discrete point at the node. The stress concentration of skeletal-P was present in the middle of the ligament, while strut-P was evenly stressed throughout the ligament in the direction of the force, leading to slightly higher mechanical properties. Instead, skeletal-IWP and strut-IWP exhibited stress concentration at the joint of the ligament. Additionally, under the identical type of TPMS conditions, skeletal-TPMS generally exhibited more significant stress concentration compared to strut-TPMS, except for the P structure. By comparing the Young's modulus and yield strength of skeletal-TPMS and strut-TPMS, it was found that the G, D, and IWP structures of skeletal-TPMS have higher stiffness and strength than strut-TPMS, while the opposite is true for the P structure. Overall, skeletal-TPMSs have a more uniform and reasonable stress distribution compared to strut-TPMSs.

Similarly, Al-Ketan et al., [88] explored the topology-mechanical property relationship between skeletal-TPMS, strut-TPMS, and sheet-TPMS using quasi-static compression, and their mechanical properties have been deduced from the corresponding compressive stress-strain responses. In general, three main deformation mechanisms can be identified when analyzing the stress-strain responses: (1) the formation of shear bands is the most prominent mechanism, occurring immediately after the peak stress, and it is observed in the Kelvin, skeletal-Diamond, sheet-Primitive, sheet-Gyroid, skeletal-IWP, Octet-truss, and sheet-Diamond structures. After the first shear band forms, layers start to fail diagonally along this band, and in some cases, a double shear band may be seen as in the Octet-truss and sheet-Diamond. (2) The second mechanism observed is the failure of horizontal layers of cells layer by layer, as happened in the skeletal-Gyroid and Gibson-Ashby structures. Finally, (3) the deformation of the sheet-IWP, where the structure deforms collectively, with every layer deforming in the same manner as its neighbors.

As mentioned earlier, also in this work, the power law (n) was used to assess the nature of the deformation of TPMS structures. The authors report that the sheet-Diamond has emerged as the topology with the best mechanical properties, with an n value of around 0.5 for stiffness, making it the least susceptible to changes in relative density. It surpasses the well-known Octet-truss, which has a stretching-dominated behavior, as indicated by its n value of 1.23. Among the other sheet-TPMS structures, the n values for stiffness suggest a near stretching-dominated behavior, with values ranging from 1.15 to 1.31. Interestingly, the power law index of the sheet-based Gyroid is similar to that of the Octet-truss. Meanwhile, the Kelvin and Gibson-Ashby strut-based structures exhibit a mixed mode of deformation, as indicated by their n values of 1.56 and 1.62, respectively. The same can be said for the skeletal-Gyroid, which has an exponent of 1.68. The skeletal-Diamond and skeletal-IWP, on the other hand, exhibit a bending-dominated mode of deformation, with n exponent values greater than 2.

A noteworthy observation can be made regarding the peak and plateau stress, as well as the toughness of the cellular structures that were tested. The results showed that the topologies based on sheet-TPMS had a peak stress that was 1.3 to 2 times higher than the peak stress achieved using the skeletal and strut approach for all TPMS topologies. Additionally, these topologies also had higher toughness values compared to the other two classes.

Ultimately, predicting the properties of 3D-printed TPMS-based lattices is essential to mitigate the printing deviations that can occur during the printing process and to understand the material-topology-property relationship. Finite element analysis (FEA) has been widely used to investigate these features. It can be employed to obtain the ideal behavior

of lattices under mechanical loading, allowing for an objective comparison between different types of lattices. Dalaq et al., [89] studied the effect of architecture, volume fraction, and modular ratio on the effective elastic properties of sheet-based TPMS topologies. Their results showed that the impact of the architecture is more pronounced when the contrast in the modular ratio is high.

Al-Ketan et al., [90] used an elastic-perfectly plastic constitutive model to compare the mechanical properties of sheet-TPMS and strut-TPMS lattices. Plastic strain distribution revealed that sheet-based lattices exhibit the least localization of plastic deformation, which suggests delayed damage and fracture compared to strut-based lattices. Several other studies have also conducted FEA using simple elastic-perfectly plastic constitutive models to predict the elastic and yield properties of TPMS-based lattices [90–93].

However, to fully understand the material-topology-property relationship for large deformations, more complex constitutive models calibrated based on the properties of the base materials are necessary. Only a few studies have used more realistic constitutive models to study the large deformation behavior of TPMS-based lattices, such as the plastic model within the FEA package Abaqus with isotropic hardening used to capture the post-yield properties of sheet-networks lattices. For instance, Abueidda et al., [94] used more complicated and accurate finite deformation constitutive models to investigate the mechanical properties of polymeric sheet-networks TPMS lattices, concluding that the hyperelastic-viscoplastic model predicts experimental results better than the elastic-viscoplastic model.

Despite the numerous numerical simulations performed to gain insights into the mechanical behavior of TPMS-based lattices, nonconformity between the numerical and experimental results is often observed due to defects introduced during the fabrication process. To reduce this nonconformity, Zhang et al., [95] accounted for the porosity-rich surface layers by uniformly reducing the sheet's thickness in the CAD model. However, this approach relies on trial and error to arrive at the best thickness reduction to be incorporated. Alternatively, more sophisticated material constitutive models can be used, or more realistic CAD models, that account for the defects introduced during the fabrication process, can be reconstructed from CT-scan images.

3.2. Permeability performance

Permeability is a parameter that quantitatively measures the ability of a porous medium to conduct fluid flow, and it depends on the combination of porosity, pores size, orientation, tortuosity, and interconnectivity [96]. For tissue-engineered scaffolds, permeability is a determinant factor as it plays a significant role in the ability of cells to penetrate the porous media and for nutrients to diffuse. Instead, for bone regeneration, permeability is essential because higher values are believed to improve bone ingrowth and because inadequate values may induce the formation of cartilaginous tissue instead of bone. As discussed before, since TPMS are highly interconnected porous architectures, they can be designed to have a significant impact on permeability. However, precisely predicting and evaluating the TPMS permeability is still an open challenge.

In general, as reported by Dias et al., [96] the permeability can be tuned by changing the porosity as well as the size of the unit cell. As a proof of concept, nine different structures were studied in this study, all with the same geometry but with different unit cell sizes (1, 1.4, and 1.7 mm) combined with three degrees of porosity (30%, 50%, and 70%). The permeability results show an expected increase with increased porosity and an increase with the size of the unit cell. This is explained by the fact that to achieve the same porosity, there will be bigger pores in bigger unit cells, leading to higher permeability values. However, such a study does not consider other effects related to the material surface, like wettability and roughness, and features like the radial flow.

To this end, Montazerian et al., [97] discussed the influence of pore shape on longitudinal and radial permeability using strut-based and surface-based TPMS structures. This aspect is most important for cell-landed scaffolds since it is recognized that cell penetration into the scaffolds mainly occurs radially. Thereby, the radial permeability must be taken into account in the design procedure.

Results on longitudinal permeability highlighted that it depends on pore architecture and that TPMSs are generally more prominent in fluid flow conduction than strut-based geometries. Specifically for the latter, the rhombic dodecahedron and octahedron are the weakest structures in conducting fluid flow, while diamond and hexahedral structures are the most permeable architectures. Instead, the TPMS primitive structure is the least permeable compared to the diamond and gyroid ones. The gyroid is the most permeable for all porosity values.

The change in the flow direction from the longitudinal to radial flow highly affects permeability for all structures. Numerically it has been found that radial permeability was roughly half of the longitudinal permeability. Diamond and hexahedral structures showed less sensitivity to the flow direction, thus leading to increased radial permeability. In other words, as reported by the authors, the more longitudinally permeable structures are also the more permeable ones in the radial flow direction.

The superior permeability for TPMS-based structures, particularly of gyroid, was already proven by Melchels et al., [98], where a 10-fold improvement was reported relative to a non-stochastic scaffold.

The higher permeability of TPMS-based scaffolds compared to non-stochastic ones significantly improved the wetting properties and increased the settling speed of cells upon static seeding of immortalized mesenchymal stem cells. Furthermore, the TPMS-based scaffold further enhances the transport of oxygen and nutrients throughout it. It creates tissue engineering grafts with a designed, pre-fabricated vasculature, which is impossible to obtain with lattice and non-stochastic structures.

However, to date, no experimental work has been conducted to scrutinize the cell radial permeability on patterned porous scaffold structures. Hence, biological assessments should be experimentally conducted to compare the actual cell growth behavior with such theoretical results.

Lastly, we would like to emphasize that although the permeability (either longitudinal or radial) can be improved by higher porosity, the mechanical performances of TPMS will be weakened. Hence, a reasonable trade-off between mechanical properties and permeability will need to be made according to diverse application requirements.

4. Manufacturability of TPMS

Although TPMS geometries were discovered over a century ago, their fabrication was an intricate task hindered by the limitations of conventional manufacturing techniques. Recent advancements in AM techniques facilitated this task. They allowed for the fabrication of TPMS geometries over various length scales and materials, including metals, polymers, composites, and ceramics. In an attempt to study the multi-functional features of TPMS, several AM techniques have been employed, such as powder bed fusion (PBF), stereolithography appearance (SLA), digital light processing (DLP), and fused filament fabrication (FFF). For detailed information about these different techniques, the reader is directed to the following comprehensive review articles [99–101]. Although the abovementioned AM techniques can conveniently fabricate TPMS structures, complex porous topologies (i.e., graded, hybrid, or multiscale) manufactured using soft materials as feedstock are still challenging to obtain, considering the precision and efficiency of current AM technologies.

This section summarizes these techniques and the associated materials and discusses the effect of each process on the manufacturability of such TPMS-based lattices.

When selecting a process for producing TPMS, consider that macro-fabrication is efficient for producing functional TPMS using various

materials, including polymers, metals, ceramics, and composites. In contrast, micro/nano-fabrication can produce microscale TPMSs with nanoscale features but is currently limited to a few polymeric materials. Furthermore, as discussed in the following paragraphs, PBF can fabricate TPMSs with polymers and metals without defects. However, such a technique leads to many bonded particles on the TPMS surfaces, which can increase the surface roughness of the structures and thus compromise bone tissue regeneration. The SLA, although limited to polymeric materials, it is capable of achieving smaller wall thickness and strut diameters than what can be obtained with other available techniques. Instead, the precision of material extrusion AM, like FFF, is much lower than SLA or PBF but can be adapted to many polymeric and composite materials. One drawback of such technology in fabricating TPMS is the presence of defects, irregularities, sagging, and debris. These drawbacks are highly

dependent on various processing parameters. Nanofabrication captures TPMS design with minimal deviation and pore sizes. However, such a technique is significantly limited by scalability compared to the techniques mentioned above.

4.1. Macro-fabrication

4.1.1. Powder bed fusion (PBF)

Selective laser melting (SLM) and selective laser sintering (SLS) are the most commonly used PBF techniques to fabricate metal or polymer TPMS structures. The powder materials are melted or sintered, layer-by-layer, utilizing an energy source (e.g., laser or electron beam).

The PBF techniques were used to produce TPMS-based lattices using a wide range of materials (Fig. 5). For instance, Yan et al., [102] dis-
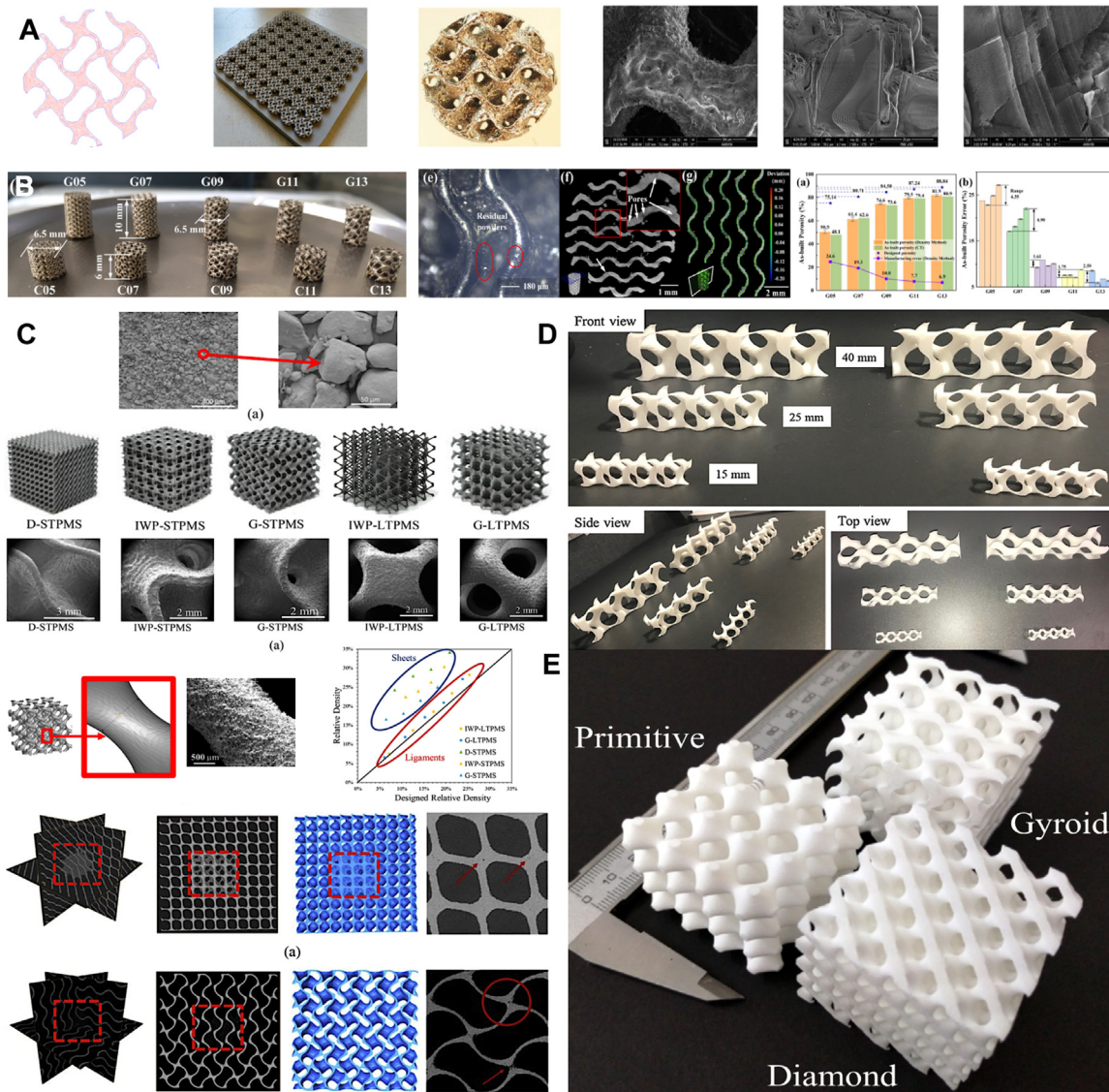

Fig. 5. A) Hatching and contour slices used for creating the laser scanning paths and porous TPMS fabricated with titanium powder, and relative SEM images. Reproduced with permission from Ref. [103]. CC BY 4.0 B) SLM-built gyroid samples of 316 l powders (top). Measured and designed porosities of as-built samples (center) and comparisons between fabricated and designed TPMS structures using optical microscopy, CT, and CAD data (bottom). Reproduced with permission from Ref. [104]. CC BY 4.0. C) SEM image of PA 1102 5 × 5 × 5 TPMS lattices with a 8 mm cell size fabricated by SLS technique. These images show the printing quality of the lattices. In the center-left of the image, deviation between designed and fabricated 3 × 3 × 3 arrays: they are designed with a minimum diameter of 1.37 mm while the SEM image shows a minimum diameter of 1.54 mm. In the centre-right, designed relative density versus measured relative density for the TPMS. In the bottom, CT scan images and its corresponding slices of reconstructed CT scan images showing the entrapped powder (right) and microvoids (left). Reproduced with permission from Ref. [105]. CC BY 4.0 D) Prototype samples of gyroid lattices of 15, 25, and 40 mm unit cell size with 4 × 1 × 1 periodicity. Fabrication is made with SLS using nylon-12 powder. Reproduced with permission from Ref. [106]. CC BY 4.0. E) Gyroid, diamond, and primitive lattice structures manufactured by SLS using polyamide PA2200. Reproduced with permission from Ref. [80]. CC BY 4.0.

cussed the manufacturability of TPMS-based lattices using the SLM technology with 316 l stainless steel powder. According to the experimental results, all the unit sizes ranging from 2 to 8 mm can be fabricated without defects and additional support structures. However, such a technique leads to many bonded particles on the surfaces of the lattice. As a result, these bonded particles increased the surface roughness of the structures. Also, Yavari et al., [103], fabricated biocompatible gyroid-based implants with pure Titanium (CP-Ti) powder for addressing unmet clinical needs in orthopedic surgery and stimulating bone tissue regeneration (Fig. 5A). The laser paths were optimized without overlapping contours. However, technical constraints are responsible for this difference between theoretical and experimental values. The relative density of the porous structure showed the SLM process has resulted in highly dense material (relative density > 28%) and porosity from micro CT of 71 ± 6.2%, compared to the 76 ± 0.2% from theoretical calculations.

Ma et al., [104] compared the SLM-fabricated TPMSs and the designed models by CT images using 316 l stainless steel powder (Fig. 5B). The authors reported that all manufactured porosities were lower than the theoretical values for each type of scaffold. The theoretical porosities ranged from 75.1-88.8%, while the manufactured porosities ranged from 50.5-81.9%. The error between theoretical and manufactured values decreased as the theoretical value increased; the manufactured errors went from 46 to 80 μm. Furthermore, as depicted in Fig. 5B, the authors showed the manufactured defects of such structures, such as residual powders and internal pores, presenting the deviations between the CAD and CT data, which indicated that the manufactured thickness was bigger than the assigned theoretical value.

On the other hand, the PBF technique, particularly SLS, is also used to fabricate TPMS-based metamaterials using thermoplastic nylon polymeric powder. Abou-Ali et al., [105] fabricated ligament- and sheet-based TPMS topologies (namely, diamond, I-WP, and gyroid) using PA1102 material with a particle size of approximately 50 μm (Fig. 5C). The relative density of all printed structures was close to the designed one, and the SEM analysis indicated an optimized printing quality of the current topologies. However, CT scans performed on the gyroid, and diamond sheet lattices highlighted microvoids and internal defects in the bulk of the samples and within the network of pores. Instead, Elmadih et al., [106] utilized nylon-12 powder for fabricating 20% volume fraction gyroid-based lattices with cell sizes of 15 mm, 25 mm, and 40 mm, using the SLS technology (Fig. 5D). Compared with the original digital model, the maximum cell size and volume fraction deviation are 1.8% and 10%, respectively, and the mass of the fabricated lattices was lower by 4.9%, 2.1%, and 0.3% in lattice with cell sizes of 15 mm, 25 mm, and 40 mm, respectively.

Maskery et al., [80] used the EOS polyamide PA2200, also based on the nylon-12, to manufacture a $4 \times 4 \times 4$ arrangement of primitive, gyroid, and diamond porous structures (Fig. 5E). By fine-tuning the SLS processing parameters (i.e., laser power, laser scan speed, laser hatch spacing, and powder deposition thickness), the volume fractions of the TPMSs were very consistent, providing a mean of 0.294 ± 0.007, very close to the theoretical value (i.e., 0.3).

Overall, although through PBF technologies, it is possible to use different types of material (from metals to polymers), there are still some drawbacks to face. One concern is the deviation between theoretical and actual relative density. As we reported, in some cases, the fabricated samples show higher relative densities, while in others, they are lower than the theoretical values. The deviation from design could be attributed to several factors. (1) Oversizing or undersizing of the strut diameter in the case of strut-TPMS or sheet thickness in the case of sheet-based TPMS, which is related to the melt pool size, laser spot size, powder particle size, and amount of defects in the 3D-printed lattice. (2) Internal fabrication defects, like voids or cracks, caused by the solidification process associated with laser additive manufacturing. As previously discussed, it can be characterized through computed tomography scanning. (3) Sticking powder on parts of the sintered component that can increase its weight.

Another concern is the stair-stepping effect. Although TPMS are described with a smooth-curved topology, SEM images of the additively manufactured lattices reveal a staircase-like profile (Figs. 5A-C). This observation is strictly related to the layer-by-layer building approach of AM techniques. When a CAD file is prepared for fabrication, it gets sliced into two-dimensional layers built upon each other to form the 3D components. As such, the effect of slicing is observed as a staircase-like profile for any curved surface. In general, the layer thickness depends on the particle size and distribution of the base powder. Such a problem can be overcome using small layer thickness results in reducing the staircase effect; however, it increases the build time. Therefore, optimizing the printing parameters to obtain the best representation of the desired component is crucial.

### 4.1.2. Stereolithography appearance (SLA) and digital light processing (DLP)

The SLA is utilized to cure photosensitive liquid material on a moving building tray with an ultraviolet (UV) laser source. The designed models can be fabricated with high accuracy by controlling the light spot size, which determines the printing resolution. Due to the limitation of the fabrication principle, only a tiny amount of material with photosensitive properties can be utilized by SLA. However, it can achieve smaller wall thicknesses and strut diameters than the currently available PBF 3D printers.

Ullah et al., [107] fabricated calcium phosphate nanoparticles with gyroid-based structures as bio-functional scaffolds for bone repair. The bio-functional elements, including Mg, Sr, and Zn, have been doped into these calcium phosphate nanoparticles and merged with photosensitive resin. Using SLA, the wall thicknesses and pore sizes of TPMS printed structures were 300 and 500 μm, respectively.

Of particular interest, Elomaa et al., [108] used poly(ϵ-caprolactone) (PCL) to manufacture TPMS scaffolds through SLA. The PCL is a well-studied, highly biocompatible polymer with a low melting temperature. Due to its biocompatibility, PCL still is used in tissue engineering and regenerative medicine. However, PCL-based scaffolds are not thoroughly investigated using AM techniques, except for some recent works [109,110]. The authors reported that the TPMS scaffolds precisely matched the CAD designs, with no observable material shrinkage. The average porosity measured by μCT was 70.5 ± 0.8%, which is very close to the designed 70% porosity, and the average pore size was 465 μm.

Yu et al., [111] fabricated uniform and graded Schwarz-P and gyroid structures using a commercially available resin (FLGPWH04). The author reported that the wall thickness accuracy was higher than 94%, and the maximum weight deviation among the four structures was 2.89%. Concerning the porosity, the maximum deviation was 1.41% from the designed model (Fig. 6A).

On the other hand, the DLP technology is developed based on the fabrication principle of SLA. Differently, the liquid material is curved point by point by SLA to generate the whole structure. Yet, each sliced layer of structures is directly cured by DLP in each projection step. DLP can significantly improve manufacturing efficiency. However, limited by the resolution of the projection equipment, the DLP fabrication sizes of the structures are smaller than SLA. Although it is not widely used, in recent years, the DLP proved to be a great choice to precisely fabricate TPMS porous structures with novel properties and functionalities like superhydrophobic, self-cleaning, or anti-biofouling [118–120]. To demonstrate the design flexibility of DLP, Dong et al., [112] printed a broad range of various 3D shapes (Fig. 6B) from complex-shaped structures (gyroid, spherical lattice, boat, propeller) with printing resolution from 50 μm to 500 μm. In doing so, the authors selected ink consisting of a hydrophobic butyl acrylate (BA, 30 wt%), ethylene glycol dimethacrylate (EDMA, 20 wt%), 1-decanol (50 wt%), and Irgacure 819 as the monomer, crosslinker, porogen, and photoinitiator, respectively. In another study, Dong et al., [113] introduced a method combining the advantages of 3D printing via DLP and polymerization-induced phase separation, which enables the formation of 3D polymer structures of digi-
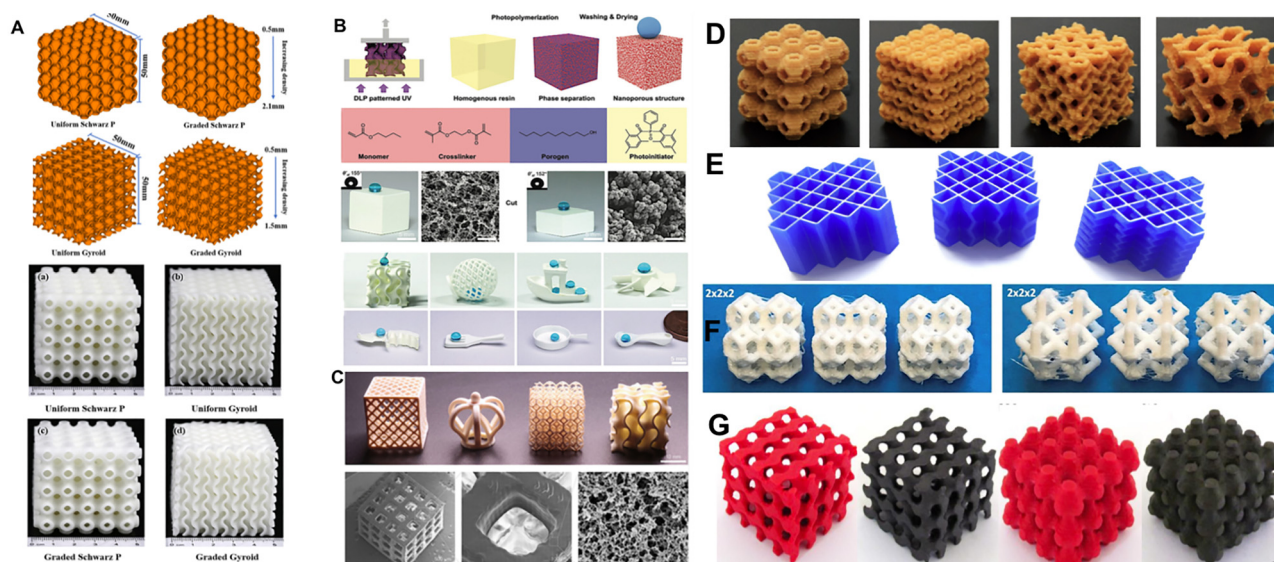
Fig. 6. A) CAD models and related printed samples of uniform and graded Schwarz-P and Gyroid's structures. Reproduced with permission from Ref. [111]. CC BY 4.0. B) Schematic showing the DLP 3D-printing process using phase-separating ink and relative chemical structures. Photographs of dyed water droplets on the surface of a 3D-printed cube with superhydrophobic properties and complex-shaped 3D-printed superhydrophobic objects. Reproduced with permission from Ref. [112]. CC BY 4.0. C) Examples of 3D-printed structures (i.e., hollow mesh box, a crown, a lattice cube, and a gyroid, C-top) and SEM micrographs of a 3D-printed lattice with 250 μm square pores (C-bottom). Reproduced with permission from Ref. [113]. CC BY 4.0. D) 3D-printed TPMS structures using PLA polymer filament. Reproduced with permission from Ref. [114]. CC BY 4.0. E) FFF printed origami soft-like honeycombs. Reproduced with permission from Ref. [115]. CC BY 4.0. F) 3D-printed arrays body-centered cubic (BCC) and Kelvin arrays, using TPU 95 shore A filament. Reproduced with permission from Ref. [116]. CC BY 4.0. G) 3D-printed gyroid- and primitive-based TPU structures before (in red) and after the graphene dip-coating process (in black). Reproduced with permission from Ref. [117]. CC BY 4.0.

tally defined macroscopic geometry with controllable inherent porosity at the sub-micrometer scale (Fig. 6C). The authors demonstrated the possibility of creating 3D polymer structures of highly complex geometries and spatially controlled pore sizes from 10 nm to 1000 μm, which has always been challenging for AM technologies.

DLP and lithography-based manufacturing technology are also widely used for additively manufactured TPMSs made from ceramic materials for bone implant applications. Vijayavenkataraman et al., [121] fabricated uniform Schwarz-P structures with thickness and unit cell size ranging from 0.2-0.7 mm and 1.5-3.5 mm, respectively, using ceramic Alumina (Al_2O_3) as feedstock material. The authors reported the presence of defects when structures were examined using SEM. For example, residual particles were found attached to the fabricated structures. Such particles are probably caused by the trapped ceramic powder inside the structure, which was not completely removed during the post-processing. This contributes to the thickness and weight variations and increases local surface roughness. Also, cracks can be seen in all tested structures. The formation of cracks might be due to the stresses arising in the material during thermal treatment. As highlighted by the authors, cracks are unavoidable in ceramic structures, and these cracks are challenging to be closely controlled during fabrication.

Shen et al., [122] printed four different TPMS structures (i.e., primitive, gyroid, IWP, and s14) *via* the DLP technique using zirconia (ZrO_2) as the raw material. The authors reported that the real density is always much higher than the designed density for all the studied ceramic TPMS structures. In most cases, the real density is about twice the designed density because the light is scattered during printing. As commonly known, light scattering within the ceramic filled causes a certain amount of overgrowth of dimensions in the final geometry. In addition, all printed structures showed defects in all curved paths since the local arc is simulated by several square light spots, leading to some influence on the final mechanical behavior.

Interestingly, the high solid loading and viscosity of ceramic slurry limit the broader use of DLP in producing porous ceramic TPMS scaffolds. Li et al., [123] utilized the top-down DLP system to overcome this issue and achieve ceramic-resin slurry with high solid loading. Unlike standard DLP printers, they printed TPMSs with a light source placed

above the tank using photosensitive β-TCP/BG-resin slurries with various solid loadings. Using such a method, the light can directly reach the photosensitive material. Compared with the TPMS structures fabricated by DLP, the volume will further be reduced after sintering. Based on the proposed methods, TPMS structures can be precisely fabricated as bone scaffolds. The results showed that the maximum viscosity of the β-TCP/BG-resin slurry for the top-down DLP technique was 85.92 Pa • s with a solid loading of 60% wt. The curing depth exceeds 100 μm at each solid loading after 18000 ms irradiation time. In addition, the shaping error and sintering shrinkage of the porous structure were estimated. It was found that the pore size and sintering shrinkage reached a minimum value for the scaffolds fabricated by the slurry of 60% wt. The compressive strength of the β-TCP/BG scaffolds increased with the solid loading, reaching a maximum value of 11.43 ± 0.4 MPa for the solid loading of 60% wt.

4.1.3. Fused filament fabrication (FFF)

The FFF technology is one of the most widely used material extrusion AM techniques. As a method of material extrusion technology, the precision of FFF is much lower than SLA or PBF. Until recently, this technology was not an ideal choice for fabricating porous TPMS structures for several reasons. (1) The need for support structures for hanging TPMS surfaces; thus, the surface quality is further affected after removing support structures. (2) It generates cracks and voids between layers due to improper bonding, which can impair mechanical behavior. (3) The presence of defects, irregularities, sagging, debris, and stringing and lumps of filaments inside the unit cell could negatively influence the structure's properties. (4) The typical FFF process constraints could limit the range of manufacturable TPMS topologies/shapes and sizes, especially when printing soft materials. These drawbacks are highly dependent on various processing parameters (such as nozzle diameter, printing temperature, printing speed, layer thickness, extrusion multiplier, and fan speed, among others) that can affect the material, which constitutes the TPMS structure. Therefore, when using FFF to fabricate TPMS structures, tuning these printing parameters to probe the optimum printing combination is essential. However, for some rigid polymers, such as polylactic acid (PLA) and acrylonitrile butadiene styrene (ABS),

FFF is an effective way for manufacturing TPMS as reported by Sajadi et al., [114] Mohammed et al., [117,124] and Townsend et al., [115] (Figs. 6D-E).

Conversely, Sala et al., [125] have recently demonstrated how it is possible to produce tailored soft TPMS lattices by optimizing multiple printing parameters (e.g., nozzle temperature, extrusion width, extrusion multiplier, retraction distance, retraction speed, printing temperature, and fan speed). These parameters depend not only on the type of TPMS structure but also on the unit cell size. In this study, the authors address design issues, delve into optimum printing parameters, and analyze a set of numerical parameters for the Schwartz-P, gyroid, and honeycomb structures (with unit cell sizes spanning from 3 to 12 mm). These parameters can be used for designing structures with tunable mechanical behavior, which can be a relevant possibility to be exploited in healthcare and bioengineering.

Similarly, Holmes et al., [126] reported the optimized printing parameters (e.g., nozzle diameter, extrusion multiplier, quick retraction settings, and fan speed) of flexible thermoplastic polyurethane (TPU) with 60 shore A. These parameters were used to manufacture gyroid-based metamaterials as a tunable replacement for polyurethane foams to treat or mitigate conditions like pressure ulcers or to provide personalized support structures for patients with specific clinical needs.

Graziosi et al., [116] investigated the influence of the printing process on the fabrication of body-centered cubic (BCC) and the Kelvin strut-based soft TPMS using TPU 95 shore A (Fig. 6F). The authors analyzed the experimental and numerical behavior of such structures, highlighting the importance of multiple design aspects and the printing process for overcoming issues of soft lattices due to the intrinsic complexity of printing flexible materials.

Lastly, Mohammad Ebrahim Imanian et al., [117] have recently reported the feasibility of fabricating four different TPMS soft structures (i.e., primitive, diamond, gyroid, and I-WP) to be used as soft piezoresistive wearable conductors for monitoring human bodily motions. This was possible after a facile dip-coating process of a continuous graphene layer over the TPU internal surfaces (Fig. 6G).

We also report an interesting work by Shaikh et al., [127], where the feasibility of supportless printing of lattice structures by metal fused filament fabrication (MF3) of Ti-6Al-4V was investigated for the first time. The MF3 involves a FFF process, with additional subsequent steps involving binder removal and sintering at elevated temperatures to densify the printed parts. MF3 starts with sintered metal powder, which was Ti-6Al-4V in this study, bonded in a multi-component polymer-based binder. The feedstock is then extruded to form a 1.75 mm diameter filament that can be used on an extrusion-based desktop printer to build a 3D part. The printed part is referred to as the "green part", and is subsequently subjected to debinding to remove the polymer binder, leading to a "brown part". Finally, sintering is conducted in an inert environment using H_2 or N_2 gas at elevated temperatures. This completes the cycle by providing a fully dense metal part. The authors reported that the lattice geometries required considerable changes in MF3 printing parameters compared to the standard FFF method. The printed lattices showed large deflection in unsupported overhang due to gravity. It can be considered a defect that stems from the inherent overhang feature in any lattice structure, and the amount of deflection varies with cross-section type and geometric configuration. Furthermore, to investigate how the extruded sagging in the unsupported overhang in the green part leads to sintered part quality, the unit cells were cut in the middle *z*-axis. As reported by the authors, poorly diffused and loose beads were observed in the bottom-facing surface of unsupported overhangs. In contrast, adequate diffusion and packing of densification were observed in the lower half of the cell. Despite such drawbacks that can be overcome by controlling design optimization of the part and printing parameters, it was still possible to pursue the potential of MF3 concerning both beam-based and surface-based lattices.

Overall, we are confident that more and more thorough investigations on printing parameters of printable FFF materials can be a valuable

strategy to effectively push the boundaries of such processes for multidisciplinary applications. Indeed, as we reported, optimizing the FFF printing parameters can allow a printing resolution adequate to print flexible lattice microstructures with the desired level of accuracy. Besides, it can push forwards the use of biocompatible and bioabsorbable polymers, more suitable for biomedical applications, as the feedstock is safer and easier to handle and requires no further post-processing [128]. It thus guarantees more versatility compared to, for example, the SLS or the SLA processes.

4.2. Micro/Nano-fabrication

Besides the above-mentioned AM techniques, other intriguing fabrication methods for producing microscale TPMS structures with nanoscale feature sizes have recently gained traction. Among them are direct laser writing (DLW) [129] and projection micro-stereolithography (PµSL) [130]. Thanks to these 3D printing techniques, micro-/nano-TPMS have reached an unprecedented resolution, as well as mechanical properties, including ultralightweight 99.9% air but ultrahigh stiffness, large deformability and recoverability, and ultrahigh specific strengths that approach the theoretical limits [131]. However, to date, such advanced AM techniques are limited to a few polymeric materials.

Cao et al., [132] fabricated TPMS structures by PµSL using photosensitive resin polyethylene glycol diacrylate (PEGDA). The layer thickness was only 5 µm for each sliced layer. The authors observed that, although the PµSL technique was effective in fabricating the samples, ripples and non-uniform thickness in the wall of the TPMS structures could still be observed. Furthermore, some particles of raw material were also bonded on the surfaces, which could affect the mechanical properties of the desired structure.

Instead, Al-Ketan et al., [90] employed a 3D-DLW system to fabricate both sheet- and solid-based micro-architected TPMS with relative densities of 10%, 15%, 20%, and 25% having a unit cell size of 100 µm.

Studies on 3D micro-/nano-TPMS are still in the initial stage, and many open questions remain. However, we are confident that these high-resolution AM techniques will enable the successful fabrication of micro-/nano-lattices with complex topologies with exceptional mechanical properties and performances. Thus they are opening up new avenues for the next-generation TPMS metamaterials with unprecedented properties for a broad range of applications, including biomedical devices, drug delivery, tissue engineering, lightweight structural components, energy absorption and storage, mechanical actuation, and thermal insulation.

5. Biomedical applications

The multifunctionality and tunability of TPMS-based materials are leveraged in several applications to enhance the overall performance and provide novel solutions for existing biomedical problems. Among these, TPMS structures are widely applied in the biological domain and tissue engineering as a viable strategy to fabricate biomimetic porous scaffolds, medical implants, and cell-landed grafts to repair and regenerate damaged tissues and organs.

As reported by Dong et al., [113] differently from non-porous lattice or foam structures, the TPMSs are suitable for cell attachment, migration, and proliferation. Moreover, the high-volume specific surface areas and the highly interconnected porous architectures could supply enough space to transport nutrition and waste. Using the DLP method, the authors fabricate a porous lattice with spatially controlled pore sizes from 10 nm to 1000 µm for guiding cell growth in three dimensions, resembling the complex architecture of organs. Hep G2 cells (1×10^6 cells per mL) were seeded on porous and non-porous scaffolds to evaluate the capability of the scaffolds to favor cell adhesion and proliferation. These scaffolds were then analyzed by fluorescence confocal microscopy from 1 to 4 days post-seeding (Fig. 7A). The area covered by live cells on the porous scaffold was 4 times higher than that of the non-porous
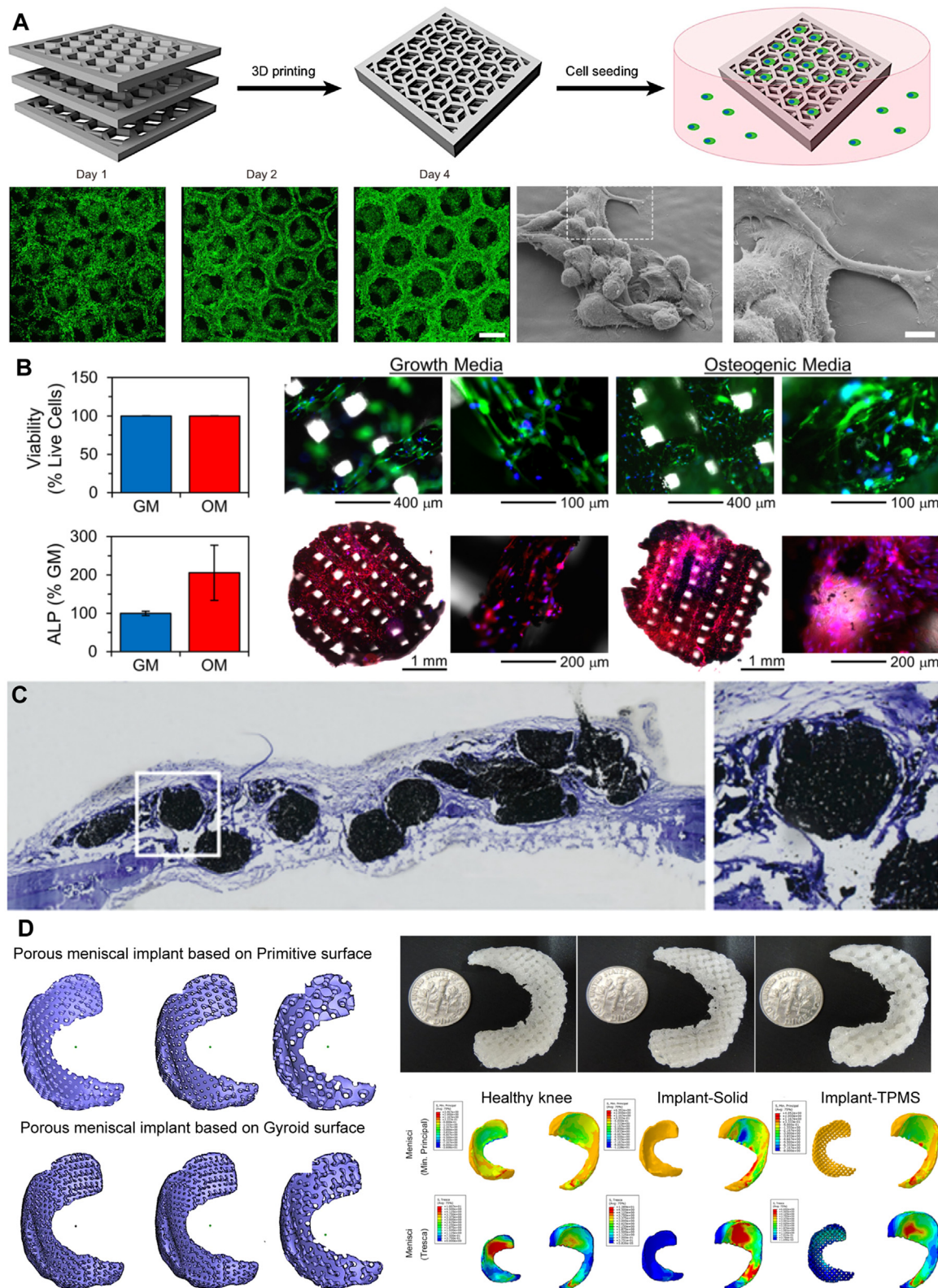
Fig. 7. A) Schematic representation of the scaffolds´ geometry from 3D printing to cell seeding. Confocal microscopy images and SEM micrographs of Hep G2 cells cultured on the porous lattice scaffold. Reproduced with permission from Ref. [113]. CC BY 4.0. B) Biocompatibility and osteogenic differentiation of hMSCs on TPMS-based structures. Reproduced with permission from Ref. [134]. CC BY 4.0. C) Histological images of calvarial defects implanted with TPMS-based bone graft substitute. Reproduced with permission from Ref. [134]. CC BY 4.0. D) Artificial porous meniscal implant designs based on the Primitive and Gyroid TPMS and related 3D-printed structures. Compression and shear stresses of the menisci for the healthy knee, the knee joint with solid meniscal implant, and the knee joint with TPMS-based meniscal implants obtained through finite element analysis. Reproduced with permission from Ref. [135]. CC BY 4.0.

one after 1 day. This result indicates a favored initial cell adhesion. The cell coverage on the lattice-based scaffold gradually increased with the extended incubation period and remained 3-fold higher than that of the non-porous scaffold. The authors also observed ~95% of cells' viability on the scaffolds during the culture period. Melchels et al., [98], to verify the advantages of TPMS structures on cell seeding and culturing, compared TPMS gyroid-based scaffolds and random foam scaffolds. With the help of the interconnected pores, the permeability of gyroid structures was 10-fold higher than random foam scaffolds due to the absence of size-limiting pore interconnections. Also, large cell populations can be found within the TPMS scaffolds after 5 days of static culture. Due to the controllable porosity of TPMS, Li et al., [133] explored the relationship between pore size and shape on the viability for cell ingrowth of different additively manufactured porous titanium scaffolds (namely, diamond, honeycomb-1, honeycomb-2, and grid). The pore sizes of the scaffolds used in this article ranged from 300 to 500 μm. NIH3T3 fibroblast cells (1×10^6 cells per 1.5 mL) were seeded on the scaffolds and analyzed 30 days post-seeding to evaluate how the pore size of different TPMS scaffolds affects cell proliferation. The authors revealed that of the four topologies used to create the scaffolds, the honeycomb-2 with a pore size of 300 μm was the only one that showed the highest cell proliferation of about 86%. Some cell proliferation was observed in honeycomb-2 with a pore size of 400 and 500 μm, but it was not as dense as the other. Instead, for the remaining topologies, no cell growth was observed.

Since some regenerative strategies require biodegradable structures that promote newly formed tissue as they degrade, Germain et al., [136] employed the FFF technique to fabricate PLA gyroid scaffolds and studied the impact of scaffold geometry and crystallinity on its degradation rate *in vitro*. Gyroid scaffolds retained their integrity upon aging in physiological conditions for 64 weeks. After that, they started to degrade drastically, with the most degraded appearing at week 84.

TPMSs have also become a promising candidate for bone defect repair in the past few years because they embody trabecular bone-mimicking hyperboloidal topography. In response to the growing popularity of TPMS scaffolds in this field, different research groups are looking out to meet all design and manufacturing criteria of TPMS scaffolds for bone regeneration [137].

For instance, Daneshmandi et al., [134] designed, fabricated, and investigated both *in vitro* and *in vivo* a TPMS-based bone graft substitute. In the *in vitro* test, the authors reported that such scaffolds are cytocompatible and induce osteogenic differentiation of human mesenchymal stem cells (hMSCs), indicated by alkaline phosphatase (Fig. 7B). No differences in cellular vitality were observed in growth media or osteogenic media, and no dying cells were observed. Even if *in vitro* data is necessary, it is not always predictive of the *in vivo* biological response. For this reason, a mouse critical-sized calvarial defect model was selected to evaluate the osteogenic efficacy of the TPMS-based bone graft substitute in an orthotopic bone site. After 8 weeks, the ability of such a 3D-printed substitute to regenerate cranial tissue within this critical-sized calvarial defect was analyzed (Fig. 7C). The histological results showed that the TPMS scaffold stimulates cellular ingrowth, retains donor cells, and induces osteogenic differentiation. Notably, the authors reported that the TPMS bone graft substitute could reabsorb and biodegrade *in vivo*, as indicated by decreased matrix mass over time. Natural bio-resorption is rare for synthetic material and suggests promise as a resorbable osteoinductive matrix. Further, no detrimental effects or accumulation were observed in vital organs. Li et al., [138] further discussed the early osteointegration of TPMS-based scaffolds made by Ti6Al4V. Such scaffolds can stimulate bone ingrowth, and, most importantly, a stable interface between TPMS implants and surrounding bone tissues after 5 weeks' implantation was obtained. Paré et al., [139] used TPMS implants to regenerate craniofacial bone defects. The authors reported that combining a 3D-printed calcium phosphate TPMS implant and cells would contribute to solving the reconstructive roadblock of craniofacial bone. Bone regeneration within the defect was evaluated, and the outcomes

were compared to a standard-care procedure. After 7 weeks, *de novo* bone formation was significantly greater in the TPMS group than in the standard control.

Zhu et al., [135] reported for the first time the use of TPMS structures based on primitive and gyroid surfaces as artificial meniscal implants after meniscectomy fabricated via FDM technology.

Compared to the standard solid meniscal implant, the TPMS meniscal implant produced lower levels of compression and shear stresses on the cartilage, thus facilitating the cartilage to retain a semilunar characteristic similar to the natural meniscus (Fig. 7D). Moreover, both compression and shear stress on the artificial cartilage was found to be sensitive to the pore properties of the meniscal implant. The meniscal implants based on primitive surfaces with a porosity of 41% showed a better performance in disseminating stresses within the knee joint. This structure has advantages in mechanics and printability, and it will benefit future custom-made clinical applications.

6. Conclusion

Nature is highly efficient in designing porous materials with unique functional features. In the past few decades, numerous attempts have been made to generate porous structures that mimic natural ones for inheriting such functional outstanding merits. Among these, TPMSs have attracted the attention of scientists for the fabrication of biomimetic porous scaffolds. As discussed in this review, the interest stems from their outstanding properties, which include mathematical controllable geometry features, highly interconnected porous architectures, tunable mechanical properties, and permeability. All these distinguishing features are of particular interest for tissue engineering and regenerative medicine applications: they enable better cell adhesion and growth, optimal integration to the surrounding tissue avoiding stress shieldings, a good permeability of fluid media and oxygen, and the possibility of vascularization.

Although the mathematical expressions and geometries of TPMSs have been studied for a long time, due to the limits of conventional manufacturing methods, TPMSs were challenging to fabricate. The rapid development of additive manufacturing promoted the prosperity of TPMS research and applications, enhancing their manufacturing at a multiscale level, from macro to micro. Also, as we reported, the feasibility of using different AM technologies allows for obtaining size programmable TPMS printable in various materials, from polymers to metal alloys.

However, challenges remain in fulfilling the demand for these bioinspired TPMS-based scaffolds in high-performance biomedical applications. Indeed, as highlighted, improper design in terms of geometry, pore size, elastic properties, interconnectivity, and anisotropy, can significantly affect the mechanical and permeability performances of TPMSs. That leads to structures with insufficient load-bearing properties or narcotic areas within the scaffold due to the lack of nutrient and oxygen supply, thus leading to cell death. Furthermore, from a manufacturing point of view, there are still some drawbacks to face, such as: 1) the deviation between the theoretical and as printed relative density (this intrinsically leads to a deviation in the weight of the TPMS, which must be taken into account for applications in which lightweight is required); 2) the possible presence of cracks, voids, defects, irregularities, sagging, and debris among TPMS structure, which can lead to an impairment of mechanical features; 3) the need for support structures for hanging TPMS surfaces (if using FFF methods); 4) the practical limits to print soft materials. As reviewed, these drawbacks are highly dependent on various processing parameters. Therefore, optimizing such parameters to obtain the best representation of the desired component is crucial. This latter needs more research attention.

Despite these, the first encouraging results in the biomedical field, reported by different research groups, indicate that TPMS architectures are potentially advantageous in repairing damaged tissues and organs and developing biodegradable materials with the desired morphology. Within TPMS structures, cells may be seeded, and then, after a period,

the resulting tissue can be transplanted into a patient. Hence, we firmly believe that outstanding 3D-printed TPMS-based scaffolds or implants with suitable geometries and performances will be generated shortly to meet the demands of the actual human biological environment and modern personalized medicine.

Declaration of Competing Interest

The authors declare no competing interest.

References

[1] Ahamed Mohammad Kaiser, Wang Hongxu, Hazell PJ. From biology to biomimicry: using nature to build better structures—a review. Constr Build Mater 2022;320.

[2] Wang Y, Naleway SE, Wang B. Biological and bioinspired materials: structure leading to functional and mechanical performance. Bioact Mater 2020;5:745–57.

[3] Ngoc San H, Guoxing L. A review of recent research on bio-inspired structures and materials for energy absorption applications. Compos B 2020;181.

[4] Scerrato D, Bersani AM, Giorgio I. Bio-inspired design of a porous resorbable scaffold for bone reconstruction: a preliminary study. Biomimetics (Basel) 2021;6.

[5] Pacheco-Torgal F, Labrincha JA. Biotechnologies and bioinspired materials for the construction industry: an overview. Int J Sustain Eng 2013;7.

[6] Natasha CH, François G, Hannachi BN. Biomimétisme en architecture. État, méthodes et outils. Les Cahiers de la recherche architecturale urbaine; 2018. p. 1.

[7] Gan Z, Turner MD, Gu M. Biomimetic gyroid nanostructures exceeding their natural origins. Sci Adv 2016;2:e1600084.

[8] Shapkin NP, Papynov EK, Panasenko AE, Khalchenko IG, Mayorov VY, Drozdov AL, et al. Synthesis of Porous Biomimetic Composites: A Sea Urchin Skeleton Used as a Template. Appl. Sci. 2021;11:8897.

[9] Badarnah L. Form follows environment: biomimetic approaches to building envelope design for environmental adaptation. Buildings 2017;7.

[10] Stammbach U. A letter of Hermann Amandus Schwarz on isoperimetric problems. Math Intell 2012;34.

[11] Schoen AH. Reflections concerning triply-periodic minimal surfaces. Interface Focus 2012;2:658–68.

[12] Schoen AH. Infinite periodic surfaces without self- intersections, Springfield, VA: Federal Scientific and Technical Information; 1970. NASA TN D-5541.

[13] Ball P. Animate materials. MRS Bull 2021;46.

[14] Feng J, Fu J, Yao X Yong H. Triply periodic minimal surface (TPMS) porous structures: from multi-scale design, precise additive manufacturing to multidisciplinary applications. Int J Extreme Manuf 2022;4.

[15] Han L, Che S. An overview of materials with triply periodic minimal surfaces and related geometry: from biological structures to self-assembled systems. Adv Mater 2018;30.

[16] Karcher H, Polthier K. Construction of triply periodic minimal surfaces. Phil Trans R Soc A 1996;354.

[17] Brakke KA. The surface evolver. Exp Math 1992;1.

[18] Gandy JF, Klinowski J. Nodal surface approximations to the zero equipotential surfaces for cubic lattices. J Math Chem 2002;31.

[19] Grosse B K. Triply periodic minimal and constant mean curvature surfaces. Interface Focus 2012;2.

[20] Longley W, McIntosh TJ. A bicontinuous tetrahedral structure in a liquid-crystalline lipid. Nature 1983;303.

[21] Andersson S, Hyde S, Larsson K, et al. Minimal surfaces and structures: from inorganic and metal crystals to cell membranes and biopolymers. Chem Rev 1988;88.

[22] Schwarz HA. Gesammelte mathematische abhandlungen, I. Springer-Verlag New York; 1970.

[23] Brakke K. The surface evolver and the stability of liquid surfaces. Phil Trans R Soc Lond A 1996;354.

[24] Lord EA, Mackay AL. Periodic minimal surfaces of cubic symmetry, 85. JSTOR; 2003.

[25] Traizet M. On the genus of triply periodic minimal surfaces. J Differ Geom 2008;2.

[26] Schoen AH. Infinite regular warped polyhedra (IRWP) and infinite periodic minimal surfaces (IPMS). Am Math Soc 1968;26.

[27] Hyde ST, O'Keeffe M, Proserpio DM. A short history of an elusive yet ubiquitous structure in chemistry, materials, and mathematics. Angew Chem Int Ed Engl 2008;47:7996–8000.

[28] Learmonth ID, Young C, Rorabeck C. The operation of the century: total hip replacement. Lancet 2007;370:1508–19.

[29] Khan B, Kumar S. Implementation of triply periodic minimal surface (TPMS) structure in mesenchymal stem cell differentiation. Res Sq 2022;1.

[30] Castro APG, Pires T, Santos JE, et al. Permeability versus design in TPMS scaffolds. Materials (Basel) 2019;12.

[31] Han SC, Lee JW, Kang K. A new type of low density material: shellular. Adv Mater 2015;27.

[32] Sharma D, Hiremath SS. Additively manufactured mechanical metamaterials based on triply periodic minimal surfaces: performance, challenges, and application. Mech Adv Mater Struct 2021;29.

[33] Abueidda DW, Bakir M, Al-Rub Rashid KA, et al. Mechanical properties of 3D printed polymeric cellular materials with triply periodic minimal surface architectures. Mater Des 2017;122.

[34] Qin Z, Dimas L, Adle D, et al. Biological materials by design. J Phys Condens Matter 2014;26.

[35] Sumpter BG, Vasudevan RK, Potok T, et al. A bridge for accelerating materials by design. NPJ Comput Mater 2015;1.

[36] Yeo J, Jung GS, Martín-M Francisco J, et al. Materials-by-design: computation, synthesis, and characterization from atoms to structures. Phys Scr 2018;93.

[37] Al-Ketan O, Al-Rub RKA. Multifunctional mechanical metamaterials based on triply periodic minimal surface lattices. Adv Eng Mater 2019;21.

[38] Lambert CA, Radzilowski LH, Thomas EL. Triply periodic level surfaces as models for cubic tricontinuous block copolymer morphologies. Philos Trans R Soc Lond Ser A 1996;354.

[39] Wohlgemuth M, Yufa N, Hoffman J, et al. Triply periodic bicontinuous cubic microdomain morphologies by symmetries. Macromolecules 2001;34.

[40] Wang S, Chern A. Computing minimal surfaces with differential forms. ACM Trans Gr 2021;40.

[41] Joaquín P. A new golden age of minimal surfaces. AMS 2017;64.

[42] Bonatti C, Mohr D. Mechanical performance of additively-manufactured anisotropic and isotropic smooth shell-lattice materials: simulations & experiments. J Mech Phys Solids 2019;122.

[43] Ian Maskery, Parry LA, Padrão; D, et al. FLatt Pack: a research-focussed lattice design program. Addit Manuf 2022;49.

[44] Al-Ketan O, Al-Rub A, MSLattice RK. A free software for generating uniform and graded lattices based on triply periodic minimal surfaces. Mater Des 2021;3.

[45] Zhao M, Zhang DZ, Liu F, et al. Mechanical and energy absorption characteristics of additively manufactured functionally graded sheet lattice structures with minimal surfaces. Int J Mech Sci 2020;167.

[46] Zhao M, Li Xi, Zhang DZ, et al. TPMS-based interpenetrating lattice structures: design, mechanical properties and multiscale optimization. Int J Mech Sci 2023;244.

[47] Li D, Liao W, Dai N, et al. Optimal design and modeling of gyroid-based functionally graded cellular structures for additive manufacturing. Comput Aided Des 2018;104.

[48] Novak N, Al-Ketan O, Borovinšek M, et al. Development of novel hybrid TPMS cellular lattices and their mechanical characterisation. J Mater Res Technol 2021;15.

[49] https://ntopology.com/.

[50] https://gen3d.com.

[51] Perez BF, Barzegari M, Geris L. A flexible and easy-to-use open-source tool for designing functionally graded 3D porous structures. Virtual Phys. Prototyp. 2022: 17.

[52] Jones A, Leary M, Bateman S, et al. TPMS Designer: a tool for generating and analyzing triply periodic minimal surfaces. Softw Impacts 2021;10.

[53] Hsieh MT, Valdevit L. Minisurf—a minimal surface generator for finite element modeling and additive manufacturing. Softw. Impacts 2020;6.

[54] Karakoç A. RegionTPMS—region based triply periodic minimal surfaces (TPMS) for 3-D printed multiphase bone scaffolds with exact porosity values. SoftwareX 2021;16.

[55] Yang N, Song Y, Huang J, et al. Combinational design of heterogeneous lattices with hybrid region stiffness tuning for additive manufacturing. Mater Des 2021;209.

[56] Veloso F, Gomes F J, Morais P, et al. Overview of methods and software for the design of functionally graded lattice structures. Adv Eng Mater 2022;24.

[57] Zhang X, Jiang L, Yan X, et al. Revealing the apparent and local mechanical properties of heterogeneous lattice: a multi-scale study of functionally graded scaffold. Virtual Phys. Prototyp. 2022;18.

[58] Günther F, Wagner M, Pilz S, et al. Design procedure for triply periodic minimal surface based biomimetic scaffolds. J Mech Behav Biomed Mater 2022;126.

[59] Meyer PP, Bonatti C, Tancogne D T, et al. Graph-based metamaterials: deep learning of structure-property relations. Mater Des 2022;2234.

[60] Yoo D. New paradigms in hierarchical porous scaffold design for tissue engineering. Mater Sci Eng C Mater Biol Appl 2013;33:1759–72.

[61] Jiawei F, Fu J, Shang C, et al. Efficient generation strategy for hierarchical porous scaffolds with freeform external geometries. Addit Manuf 2020;31.

[62] Li Y, Xia Q, Yoon S, et al. Simple and efficient volume merging method for triply periodic minimal structures. Comput Phys Commun 2021;264.

[63] Jones A, Leary M, Bateman S, et al. Parametric design and evaluation of TPMS-like cellular solids. Mater Des 2022;221.

[64] Feng J, Liu B, Lin Z, et al. Isotropic porous structure design methods based on triply periodic minimal surfaces. Mater Des 2021;210.

[65] Vijayavenkataraman S, Zhang L, Zhang S, et al. Triply periodic minimal surfaces sheet scaffolds for tissue engineering applications: an optimization approach toward biomimetic scaffold design. ACS Appl Bio Mater 2018;1:259–69.

[66] Yang N, Quan Z, Zhang D, et al. Multi-morphology transition hybridization CAD design of minimal surface porous structures for use in tissue engineering. Comput Aided 2014;56.

[67] Hu J, Wang S, Li B, et al. Efficient representation and optimization for TPMS-based porous structures. IEEE Trans Vis Comput Gr 2020;1.

[68] Strömberg N. A new multi-scale topology optimization framework for optimal combinations of macro-layouts and local gradings of TPMS-based lattice structures. Mech Based Des Struct Mach 2022;1.

[69] Luo Y, Sigmund O, Li Q, et al. Topology optimization of structures with infill-supported enclosed voids for additive manufacturing. Addit Manuf 2022;55.

[70] Wu J, Sigmund O, Groen JP. Topology optimization of multi-scale structures: a review. Struct Multidiscip Optim 2021;63.

[71] Lehder EF, Ashcroft IA, Wildman RD, et al. A multiscale optimisation method for bone growth scaffolds based on triply periodic minimal surfaces. Biomech Model Mechanobiol 2021;20.

[72] Yeranee K, Rao Y. A review of recent investigations on flow and heat transfer enhancement in cooling channels embedded with triply periodic minimal surfaces (TPMS). Energies 2022;15.

[73] Catchpole S S, Sélo RRJ, Davis AW, et al. Thermal conductivity of TPMS lattice structures manufactured via laser powder bed fusion. Addit Manuf 2019;30.

[74] Qureshi ZA, BurhanAl-Omari SA, Emad E, et al. Using triply periodic minimal surfaces (TPMS)-based metal foams structures as skeleton for metal-foam-PCM composites for thermal energy storage and energy management applications. Int Commun Heat Mass Transf 2021;124.

[75] Qureshi ZA, BurhanAl-Omari SA, Elnajjar E, et al. Nature-inspired triply periodic minimal surface-based structures in sheet and solid configurations for performance enhancement of a low-thermal-conductivity phase-change material for latent-heat thermal-energy-storage applications. Int J Therm Sci 2022;173.

[76] Yin H, Tan D, Wen G, et al. Crashworthiness analysis and optimization design of TPMS-filled structure. Int J Crashworthiness 2022;27.

[77] Wang H, Tana D, Liu Z, et al. On crashworthiness of novel porous structure based on composite TPMS structures. Eng Struct 2022;252.

[78] Maskery I, Aremu AO, Parry L, et al. Effective design and simulation of surface-based lattice structures featuring volume fraction and cell type grading. Mater Des 2018;155.

[79] Gibson LJ, Ashby MJ. Cellular solids: structure and properties. Cambridge University Press; 1997.

[80] Maskery I, Sturm L, Aremu AO, et al. Insights into the mechanical properties of several triply periodic minimal surface lattice structures made by polymer additive manufacturing. Polymer 2018;152.

[81] Fu J, Sun P, Du Y, et al. Isotropic design and mechanical characterization of TPMS-based hollow cellular structures. Compos Struct 2022;279.

[82] Zhao M, Li X, Zhang Z Zhand D, et al. TPMS-based interpenetrating lattice structures: design, mechanical properties and multiscale optimization. Int J Mech Sci 2023;244.

[83] De Aquino DA, Maskery I, Longhitano GA, et al. Investigation of load direction on the compressive strength of additively manufactured triply periodic minimal surface scaffolds. Int J Adv Manuf Technol 2020;109.

[84] Yang N, Qian Z, Wei H, et al. Anisotropy and deformation of triply periodic minimal surface based lattices with skew transformation. Mater Des 2023;225.

[85] Khaleghi S, Dehnavi FN, Baghani M, et al. On the directional elastic modulus of the TPMS structures and a novel hybridization method to control anisotropy. Mater Des 2021;210.

[86] Guo X, Zheng X, Yang Y, et al. Mechanical behavior of TPMS-based scaffolds: a comparison between minimal surfaces and their lattice structures. SN Appl Sci 2019;1.

[87] Deshpande V, Ashby M, N F. Foam topology: bending versus stretching dominated architectures. Acta Mater 2001;49.

[88] Al-Ketan O, Rowshan R, Al-Rub RKA. Topology-mechanical property relationship of 3D printed strut, skeletal, and sheet based periodic metallic cellular materials. Addit Manuf 2018;19.

[89] Dalaq AS, Abueidda DW, Al-Rub RKA, et al. Finite element prediction of effective elastic properties of interpenetrating phase composites with architectured 3D sheet reinforcements. Int J Solids Struct 2016;83.

[90] Al-Ketan O, Rezgui R, Rowshan R, et al. Microarchitected stretching-dominated mechanical metamaterials with minimal surface topologies. Adv Eng Mater 2018;20.

[91] Al-Ketan O, Al-Rub RKA, Rowshan R. The effect of architecture on the mechanical properties of cellular structures based on the IWP minimal surface. J Mater Res 2018;33.

[92] Afshar M, Pourkamali A A, Montazerian H. Compressive characteristics of radially graded porosity scaffolds architectured with minimal surfaces. Mater Sci Eng C Mater Biol Appl 2018;92:254–67.

[93] Montazerian H, Davoodi E, Asadi-Eydivand M, et al. Porous scaffold internal architecture design based on minimal surfaces: a compromise between permeability and elastic properties. Mater Des 2017;15.

[94] Abueidda DW, Elhebeary M, Shiang CSA, et al. Mechanical properties of 3D printed polymeric Gyroid cellular structures: experimental and finite element study. Mater Des 2019;165.

[95] Zhang L, Feih S, Daynes S, et al. Energy absorption characteristics of metallic triply periodic minimal surface sheet structures under compressive loading. Addit Manuf 2018;23.

[96] Dias MR, Fernandes PR, Guedes JM, et al. Permeability analysis of scaffolds for bone tissue engineering. J Biomech 2012;45.

[97] Montazerian H, Zhianmanesh M, Davoodi E, et al. Longitudinal and radial permeability analysis of additively manufactured porous scaffolds: effect of pore shape and porosity. Mater Des 2017;122.

[98] Melchels FPW, Barradas AMC, van Blitterswijk CA, et al. Effects of the architecture of tissue engineering scaffolds on cell seeding and culturing. Acta Biomater 2010;6.

[99] Guvendiren M, Molde J, Soares RM, et al. Designing biomaterials for 3D printing. ACS Biomater Sci Eng 2016;2:1679–93.

[100] Ligon SC, Liska R, Stampfl J, et al. Polymers for 3d printing and customized additive manufacturing. Chem Rev 2017;117:10212–90.

[101] Pugliese R, Beltrami B, Regondi S, et al. Polymeric biomaterials for 3D printing in medicine: an overview. Ann 3D Print Med 2021;2.

[102] Yan C, H L, Hussein A, D R. Evaluations of cellular lattice structures manufactured using selective laser melting. Int J Mach Tools Manuf 2012;62.

[103] Amin Yavari S, Croes M, Akhavan; B, et al. Layer by layer coating for bio-functionalization of additively manufactured meta-biomaterials. Addit Manuf 2020;32.

[104] Ma Shuai, Tang Qian, Ha; Xiaoxiao, et al. Manufacturability, mechanical properties, mass-transport properties and biocompatibility of triply periodic minimal surface (TPMS) porous scaffolds fabricated by selective laser melting. Mater Des 2020;195.

[105] Abou-Ali Aliaa M, Al-Ketan Oraib, Lee; Dong-Wook, et al. Mechanical behavior of polymeric selective laser sintered ligament and sheet based lattices of triply periodic minimal surface architectures. Mater Des 2020;196.

[106] Elmadi Waiel, Syam Wahyudin P, Maskery; Ian, et al. Mechanical vibration bandgaps in surface-based lattices. Addit Manuf 2019;25.

[107] Ullah I, Cao L, Cui W, et al. Stereolithography printing of bone scaffolds using biofunctional calcium phosphate nanoparticles. J Mater Sci Technol 2021;88.

[108] Elomaa L, Teixeira S, Hakala R, et al. Preparation of poly(ε-caprolactone)-based tissue engineering scaffolds by stereolithography. Acta Biomater 2011;7.

[109] Sala R, Regondi S, Pugliese R. Design data and finite element analysis of 3D printed poly(ε-Caprolactone)-based lattice scaffolds: influence of type of unit cell, porosity, and nozzle diameter on the mechanical behavior. Eng 2022;3.

[110] Daskalakis E, Huang B, Vyas C, et al. Bone bricks: the effect of architecture and material composition on the mechanical and biological performance of bone scaffolds. ACS Omega 2022;7:7515–30.

[111] Yu S, Sun J, Jiaming B. Investigation of functionally graded TPMS structures fabricated by additive manufacturing. Mater Des 2019;182.

[112] Dong Z, Vuckovac M, Cui W, et al. 3D printing of superhydrophobic objects with bulk nanostructure. Adv Mater 2021;33:e2106068.

[113] Dong Z, Cui H, Zhang H, et al. 3D printing of inherently nanoporous polymers via polymerization-induced phase separation. Nat Commun 2021;12:247.

[114] Sajadi SM, Owuor PS, Schara S, et al. Multiscale geometric design principles applied to 3D printed schwarzites. Adv Mater 2018;30.

[115] Townsend S, Adams R, Robinson M, et al. 3D printed origami honeycombs with tailored out-of-plane energy absorption behavior. Mater Des 2020;195.

[116] Graziosi S, Ballo FM, Libonati F, et al. 3D printing of bending-dominated soft lattices: numerical and experimental assessment. Rapid Prototyp J 2022;28.

[117] Imanian ME, Kardan H M, Nasrollahi F, et al. 3D printed flexible wearable sensors based on triply periodic minimal surface structures for biomonitoring applications. Smart Mater Struct 2022;1.

[118] Furstner R, Barthlott W, Neinhuis C, et al. Wetting and self-cleaning properties of artificial superhydrophobic surfaces. Langmuir 2005;21:956–61.

[119] Wang L, Gong Q, Zhan S, et al. Robust anti-icing performance of a flexible superhydrophobic surface. Adv Mater 2016;28:7729–35.

[120] Mertaniemi H, Jokinen V, Sainiemi L, et al. Superhydrophobic tracks for low-friction, guided transport of water droplets. Adv Mater 2011;23:2911–14.

[121] Vijayavenkataraman S, Kuan LY, Lu WF. 3D-printed ceramic triply periodic minimal surface structures for design of functionally graded bone implants. Mater Des 2020;191.

[122] Shen M, Qin W, Xing B, et al. Mechanical properties of 3D printed ceramic cellular materials with triply periodic minimal surface architectures. J Eur Ceram Soc 2021;41.

[123] Li X, Zhang H, Shen Y, et al. Fabrication of porous β-TCP/58S bioglass scaffolds via top-down DLP printing with high solid loading ceramic-resin slurry. Mater Chem Phys 2021;267.

[124] Mohammed MI, Gibson I. Design of three-dimensional, triply periodic unit cell scaffold structures for additive manufacturing. J Mech Des 2018;140.

[125] Sala R, Regondi S, Graziosi S, et al. Insights into the printing parameters and characterization of thermoplastic polyurethane soft triply periodic minimal surface and honeycomb lattices for broadening material extrusion applicability. Addit Manuf 2022;58.

[126] Holmes DW, Singh D, Lamont R, et al. Mechanical behaviour of flexible 3D printed gyroid structures as a tuneable replacement for soft padding foam. Addit Manuf 2022;50.

[127] Shaikh Q, Graziosi S, Atre SV. Lattice structures by metal fused filament fabrication (MF3) of Ti-6Al-4V: design and analysis. Rapid Prototyp J 2021;27.

[128] Sala R, Regondi S, Pugliese R. Design data and finite element analysis of 3D printed poly(ε-Caprolactone)-based lattice scaffolds: influence of type of unit cell, porosity, and nozzle diameter on the mechanical behavior. Eng 2022;3.

[129] Selimis A, Mironov V, Farsari M. Direct laser writing: principles and materials for scaffold 3D printing. Microelectron Eng 2015;132.

[130] Ge Qi, Li Z, Wang Z, et al. Projection micro stereolithography based 3D printing and its applications. Int J Extreme Manuf 2020;2.

[131] Miwa M, Juodkazis S, Kawakami T, et al. Femtosecond two-photon stereo-lithography. Appl Phys A 2001;73.

[132] Cao X, Xang H, Ren X, et al. Mechanical performance and defect analysis of the imperfect micro smooth gyroid cylinder shell structure. Compos Struct 2021:273.

[133] Li B, Hesar BD, Zhao Y, et al. Design and additive manufacturing of porous titanium scaffolds for optimum cell viability in bone tissue engineering. J Eng Manuf 2020;15.

[134] Daneshmandi L, Holt BD, Arnold AM, et al. Ultra-low binder content 3D printed calcium phosphate graphene scaffolds as resorbable, osteoinductive matrices that support bone formation in vivo. Sci Rep 2022;12:6960.

[135] Zhu LY, Li L, Li ZA, et al. Design and biomechanical characteristics of porous meniscal implant structures using triply periodic minimal surfaces. J Transl Med 2019;17:89.

[136] Germain L, Fuentes CA, van Vuure AW, et al. 3D-printed biodegradable gyroid scaffolds for tissue engineering applications. Mater Des 2018;151.

[137] Dong Z, Zhao X. Application of TPMS structure in bone regeneration. Eng Regen 2021;2.

[138] Li L, Shi J, Zhang K, et al. Early osteointegration evaluation of porous Ti6Al4V scaffolds designed based on triply periodic minimal surface models. J Orthop Transl 2019;19:94–105.

[139] Pare A, Charbonnier B, Tournier P, et al. Correction to tailored three-dimensionally printed triply periodic calcium phosphate implants: a preclinical study for craniofacial bone repair. ACS Biomater Sci Eng 2020;6:1821.